



PAPER

A novel method to assess the spatiotemporal image quality in fluoroscopy

OPEN ACCESS

RECEIVED

6 October 2021

REVISED

11 November 2021

ACCEPTED FOR PUBLICATION

22 November 2021

PUBLISHED

6 December 2021

P Monnin^{1,*}, A Viry¹, J Damet^{1,2}, M Nowak¹, V Vitzthum¹ and D Racine¹¹ Institute of radiation physics (IRA), Lausanne University Hospital (CHUV) and University of Lausanne (UNIL), Rue du Grand-Pré 1, 1007 Lausanne, Switzerland² University of Otago, Christchurch, New Zealand

* Author to whom any correspondence should be addressed.

E-mail: pascal.monnin@chuv.ch**Keywords:** fluoroscopy, spatiotemporal image quality, noise equivalent quanta, detective quantum efficiency, quality controls

Original content from this work may be used under the terms of the [Creative Commons Attribution 4.0 licence](https://creativecommons.org/licenses/by/4.0/).

Any further distribution of this work must maintain attribution to the author(s) and the title of the work, journal citation and DOI.

**Abstract**

Objectives. The planar formulation of the noise equivalent quanta (NEQ) and detective quantum efficiency (DQE) used to assess the image quality of projection images does not deal with the influence of temporal resolution on signal blurring and image noise. These metrics require correction factors based on temporal resolution when used for dynamic imaging systems such as fluoroscopy. Additionally, the standard NEQ and detector DQE are determined on pre-processed images in scatter-free conditions for effective energies produced by additional aluminium or copper filters that are not representative of clinical fluoroscopic procedures. In this work, we developed a method to measure ‘frame NEQ’ and ‘frame system DQE’ which include the temporal frequency bandwidth and consider the anti-scatter grid, the detector and the image processing procedures for beam qualities with scatter fractions representative of clinical use. **Approach.** We used a solid water phantom to simulate a patient and a thin copper disc to measure the spatial resolution. The copper disc, set in uniform rectilinear motion in the image plane, assessed the temporal resolution. These new metrics were tested on two fluoroscopy systems, a C-arm and a floor-mounted cardiology, for multiple parameters: phantom thicknesses from 5 to 20 cm, frame rates from 3 to 30 fps, spatial and temporal image processing of different weights. **Main results.** The frame NEQ correctly described the image quality for different scatter conditions, temporal resolutions and image processing techniques. The frame system DQE varied between 0.38 and 0.65 within the different beam and scatter conditions, and correctly mitigated the influence of spatial and temporal image processing. **Significance.** This study introduces and validates an unbiased formulation of in-plane NEQ and system DQE to assess the spatiotemporal image quality of fluoroscopy systems.

Nomenclature

Symbol	Meaning
a_t	X-ray pulse width [ms]
AERC	Automatic exposure rate control
d	Pixel value
\bar{d}	Mean pixel value
DQE	Detective quantum efficiency
DQE_{frame}	Frame DQE
DQE_{grid}	Grid DQE
DQE_{sysframe}	Frame system DQE
$DQE_{\text{sys,xyt}}$	Spatiotemporal system DQE

DQE_{xy}	Detector DQE
DQE_{xyt}	Spatiotemporal DQE
$\Delta\bar{q}$	Radiant contrast of the sharp-edged disc [mm^{-2}]
$\Delta\bar{q}/\bar{q}$	Relative radiant contrast of the sharp-edged disc
Δx	Pixel spacing in the x -direction [mm]
Δy	Pixel spacing in the y -direction [mm]
Δt	Temporal frame spacing [ms]
ESF	Edge spread function
f	Spatial frequency [mm^{-1}]
f_t	Temporal frequency [s^{-1}]
$f_{t,Nyq}$	Nyquist temporal frequency [s^{-1}]
f_x, f_y	Spatial frequency in the x/y -direction [mm^{-1}]
$f_{x,Nyq}$	Nyquist spatial frequency [mm^{-1}]
H_t	Transfer function of the temporal recursive filter
IRF	Impulse response function
$IRF_{d,sys,frame}$	Frame system IRF expressed in pixel value units
$IRF_{q,sys,frame}$	Frame system IRF expressed in photon fluence units
$IRF_{d,sys,xy}$	Spatial component of $IRF_{d,sys,xyt}$
$IRF_{d,sys,xyt}$	Spatiotemporal system IRF expressed in pixel value units
k	Gain of the recursive temporal filter
\dot{K}_{in}	Air kerma rate at the grid input expressed in the image plane [$\mu\text{Gy}\cdot\text{s}^{-1}$]
MTF	Modulation transfer function
MTF_{frame}	Frame MTF
$MTF_{in,sys,frame}$	Frame system MTF at the grid input
$MTF_{sys,frame}$	Frame system MTF
$MTF_{sys,xy}$	Spatial component of $MTF_{sys,xyt}$
$MTF_{sys,xyt}$	Spatiotemporal system MTF
MTF_t	Temporal MTF
MTF_{xy}	Spatial presampling MTF measured without scatter
NEQ	Noise equivalent quanta
NEQ_{frame}	Frame NEQ [$\text{mm}^{-2}\text{s}^{-1}$]
$NEQ_{in,xyt}$	Spatiotemporal NEQ at the grid input [$\text{mm}^{-2}\text{s}^{-1}$]
NEQ_{xyt}	Spatiotemporal NEQ [$\text{mm}^{-2}\text{s}^{-1}$]
NPS	Noise power spectrum
$NPS_{d,frame}$	Frame NPS expressed in pixel value units [mm^2]
$NPS_{q,frame}$	Frame NPS expressed in photon fluence units [mm^2]
NPS_t	Temporal component of the spatiotemporal NPS [s]
NPS_{temp}	Temporal NPS (s)
$NPS_{d,xy}$	Spatial component of $NPS_{d,xyt}$ [mm^2]
$NPS_{q,xy}$	Spatial component of $NPS_{q,xyt}$ [mm^2]
$NPS_{d,xyt}$	Spatiotemporal NPS expressed in pixel value units [mm^2s]
$NPS_{in,q,xyt}$	$NPS_{q,xyt}$ at the grid input [mm^2s]
$NPS_{q,xyt}$	Spatiotemporal NPS expressed in photon fluence units [mm^2s]
NTF_t^2	Noise transfer function of NPS_t
NTF_{xy}^2	Noise transfer function of NPS_{xy}
φ	Photon fluence per air kerma unit [$\text{mm}^2\mu\text{Gy}^{-1}$]
q	Photon fluence at the detector [mm^{-2}]

\bar{q}	Mean photon fluence at the detector [mm^{-2}]
\bar{q}_{in}	Mean photon fluence at the grid input expressed at the detector plane [mm^{-2}]
$\dot{\bar{q}}$	Mean photon fluence rate at the detector [$\text{mm}^{-2} \text{s}^{-1}$]
$\dot{\bar{q}}_{in}$	Mean photon fluence rate at the grid input expressed at the detector plane [$\text{mm}^{-2} \text{s}^{-1}$]
SF	Scatter fraction at the detector plane
SF_{in}	Scatter fraction at the grid input
SF_{out}	Scatter fraction at the detector plane
T_p	Primary transmission of the grid
T_t	Total transmission of the grid
v	Speed [$\text{mm} \cdot \text{s}^{-1}$]

1. Introduction

The assessment of diagnostic image quality is a challenging task and consists of several subsequent steps, including the characterisation of the detection efficiency of the imaging system composed of an anti-scatter grid, the detector and image processing. Different metrics have been proposed and international standard methods have been defined for digital radiography systems. The benchmark metrics for projection radiography are: the measurement of spatial resolution and noise in terms of the presampling MTF, NPS and NEQ (Dobbins 1995, ICRU Report 54 1996, Dobbins *et al* 2006a, 2006b). Based on these metrics, the International Electrotechnical Commission has defined a methodology for calculating the DQE for digital detectors used in dynamic imaging (IEC 2008). A limitation of this approach is that the metrics are measured on pre-processed images acquired using standard x-ray beam qualities for medical diagnostic equipment (IEC 2005) obtained with additional aluminium or copper filters (RQA and RQC beam qualities). X-ray beam parameters used in clinical fluoroscopic procedures can differ from RQA and RQC standards and can change throughout the procedure with the automatic variation of tube current (mA), voltage (kV) and x-ray pulse width (Boone *et al* 1993, Anderson *et al* 2000). Additionally, image quality is influenced by scattered radiation from the patient, magnification and other sources of image degradation such as geometric blurring (Kyprianou *et al* 2005, Samei *et al* 2009). To address these challenges, we investigated the possibility of adapting the formulation of NEQ and DQE compatible to complete imaging systems with scattering material, an anti-scatter grid and a detector (Monnin *et al* 2017). Furthermore, a formulation of NEQ and DQE compatible to nonlinear image reconstruction and processing (i.e. resolution is contrast and dose dependent) was proposed in the framework of digital breast tomosynthesis (Monnin *et al* 2020).

These conventional metrics have progressively been adapted to answer the challenge of dynamic image acquisition modes and cope with the temporal structure of fluoroscopic imaging procedures. The planar NEQ and DQE ignore the temporal resolution of the signal, whereas the NPS measured in fluoroscopic frames integrates the noise over the temporal frequency bandwidth. In that case, decreasing the temporal resolution increases the correlation between consecutive frames, blurs the signal of a moving object and decreases the noise without changing the in-plane MTF measured with a static object. This incorrectly inflates the planar NEQ and DQE as the temporal resolution decreases (Rowlands 1984, Zhao and Rowlands 1997, Menser *et al* 2005). Cunningham, Moschandreou and Subotic (2001) initially addressed this problem and defined 3D spatiotemporal NPS and DQE, and a specific 2D spatial DQE corrected for the system lag determined from the temporal NPS. Akbarpour *et al* (2007) described a cascaded transfer of signal and noise in spatiotemporal quantum imaging systems, and extended the Fourier-based metrics to the time domain. Friedman and Cunningham (2006, 2009) developed a method to measure the temporal MTF in a small-signal approach using a moving slanted edge. Friedman and Cunningham (2010) then used the generalized spatiotemporal MTF and NPS to reformulate the spatiotemporal DQE in an expression which includes the decorrelation between the temporal MTF and NPS. The 3D spatiotemporal metrics give a detailed formulation of the performance of spatiotemporal imaging systems, but do not describe the 2D in-plane image quality as observable over a temporal series of frames.

This work presents the development of new metrics that could be used to characterise the efficiency of dynamic imaging systems, the ‘frame NEQ’ and ‘frame system DQE’, in-plane formulations of the spatiotemporal NEQ and system DQE that account for the temporal imaging performance of dynamic systems. These new metrics are based on a cascaded description of signal and noise transfer in a dynamic imaging system and use the two following assumptions: the detector response is uniform and thus spatially and temporally shift-invariant, and the image processing is linear for small signal variations within the images. These metrics use processed images on systems that include the anti-scatter grid, the flat panel detector and image processing

techniques such as edge enhancement, noise reduction or recursive temporal filtering. We validated the measurement procedures and the method for determining these new metrics. We then evaluated the effect of phantom thickness, field of view (FOV), phantom-to-grid distance, anti-scatter grid, frame rate, and image processing on two fluoroscopy systems.

2. Theory

We consider a dynamic imaging system composed of a flat panel detector, an anti-scatter grid and image processing. Even if flat panel detectors produce a signal proportional to the input dose, the algorithms used in spatial and temporal processing applied to the images can be nonlinear. A fluoroscopy system therefore fulfils the Fourier linearity requirement only under a small-signal approach achieved within a small range of dose and signal variations within the images (small contrasts). The new metrics we are proposing derive from the method presented in Monnin *et al* (2020) to assess the imaging performance in the frequency (Fourier) domain, using the approximation of a stationary and spatially invariant imaging system considered linear in a small-signal approximation. A low-contrast copper disc was thus used as a semi-transparent edge to produce a small signal impulse in a homogeneous background in order to measure the spatial and temporal MTFs (Friedman and Cunningham 2009). In these conditions, the pixel values d depend linearly on the photon fluence q at the detector, with a gain $\partial d/\partial q$ considered constant around the mean dose level per pixel.

$$d = \frac{\partial d}{\partial q} \cdot q. \quad (1)$$

2.1. Spatiotemporal metrics

In the following developments, the indices q and d will refer to metrics expressed in photon fluence and pixel values, respectively. The spatiotemporal resolution of fluoroscopy systems is characterised by a 3D spatiotemporal IRF. The in-plane spatial resolution and the temporal resolution are independent and can be measured separately (Bernhardt *et al* 2005, Friedman and Cunningham 2009, Dehairs *et al* 2017). Accordingly, we assume that the 3D spatiotemporal system IRF ($IRF_{d,sys,xyt}$) can be expressed as the product between independent spatial and temporal components, an 'in-plane system IRF' ($IRF_{d,sys,xy}$) measured with scatter in the xy -plane of the frames and a temporal MTF (MTF_t) expressed in the temporal frequency (f_t) space.

$$IRF_{d,sys,xyt}(f_x, f_y, f_t) = IRF_{d,sys,xy}(f_x, f_y, 0) \cdot MTF_t(f_t) = \frac{\partial d}{\partial q} \cdot IRF_{q,sys,xy}(f_x, f_y, 0) \cdot MTF_t(f_t). \quad (2)$$

The in-plane system MTF ($MTF_{sys,xy}$) is $IRF_{q,sys,xy}$ normalized by the amplitude of the impulse signal ($\Delta\bar{q}$), i.e. the number of photons attenuated in the sharp edge used to produce the impulse signal (in this study a 0.1 mm thick copper disc)

$$IRF_{q,sys,xy}(f_x, f_y) = \Delta\bar{q} \cdot MTF_{sys,xy}(f_x, f_y). \quad (3)$$

In a first approximation, $MTF_{sys,xy}$ measured on images acquired with scatter is the presampling detector MTF measured without scatter (MTF_{xy}) multiplied by $(1 - SF_{out})$, where SF_{out} is the SF at the detector plane (Monnin *et al* 2017)

$$MTF_{sys,xy}(f_x, f_y) \cong (1 - SF_{out}) \cdot MTF_{xy}(f_x, f_y). \quad (4)$$

MTF_{xy} is usually measured on pre-processed images using a static sharp-edged object. $MTF_{sys,xy}$ measured at the grid input ($MTF_{in,sys,xy}$) is determined by SF_{in} , the SF at the grid input plane (Monnin *et al* 2017)

$$MTF_{in,sys,xy} \cong 1 - SF_{in}. \quad (5)$$

The spatiotemporal NPS ($NPS_{d,xyt}$) is calculated in 3D homogenous regions of interest (ROI) according to equation (6).

$$NPS_{d,xyt}(f_x, f_y, f_t) = \frac{\Delta x \cdot \Delta y \cdot \Delta t}{N_x \cdot N_y \cdot N_t} \left| \iiint (d(x, y, t) - \bar{d}) \cdot \exp(-i2\pi(f_x x + f_y y + f_t t)) dx dy dt \right|^2, \quad (6)$$

where Δx , Δy and Δt represent the pixel spacing in the x - and y -directions, and the time sampling between consecutive frames, respectively. The variables N_x , N_y , and N_t are the number of pixels in the x - and y -directions, and the number of consecutive frames considered in the calculation of the NPS, respectively. \bar{d} is the mean pixel values of the homogenous ROI. $NPS_{d,xyt}$ is related to $NPS_{q,xyt}$ using equation (7)

$$NPS_{d,xyt}(f_x, f_y, f_t) = \left(\frac{\partial d}{\partial q} \right)^2 \cdot NPS_{q,xyt}(f_x, f_y, f_t). \quad (7)$$

The units of $NPS_{d,xyt}$ and $NPS_{q,xyt}$ are $[\text{mm}^2 \cdot \text{s}]$ and $[\text{mm}^{-2} \cdot \text{s}]$, respectively. As with IRF, the spatiotemporal NPS can be expressed as the product of independent spatial and temporal components ($NPS_{d,xy}$ and NPS_t), using the spatial and temporal noise transfer functions NTF_{xy}^2 and NTF_t^2 .

$$\begin{aligned} NPS_{d,xyt}(f_x, f_y, f_t) &= NPS_{d,xy}(f_x, f_y) \cdot NPS_t(f_t) \\ &= NPS_{d,xyt}(0, 0, 0) \cdot NTF_{xy}^2(f_x, f_y) \cdot NTF_t^2(f_t), \end{aligned} \quad (8)$$

where NTF_{xy}^2 and NTF_t^2 are the spatial and temporal NPS components normalized to 1.0 at the zero-frequency

$$NTF_{xy}^2(f_x, f_y) = \frac{NPS_{d,xy}(f_x, f_y)}{NPS_{d,xy}(0, 0)} \quad (9)$$

$$NTF_t^2(f_x, f_y) = \frac{NPS_t(f_t)}{NPS_t(0)}. \quad (10)$$

$NPS_{q,xyt}$ at the grid input ($NPS_{in,q,xyt}$) is determined by the mean photon fluence at the grid input \bar{q}_{in} and the temporal frame spacing Δt (Cunningham *et al* 2001)

$$NPS_{in,q,xyt} = \bar{q}_{in} \cdot \Delta t. \quad (11)$$

The spatiotemporal IRF and NPS define a spatiotemporal NEQ, noted NEQ_{xyt} , which represents the photon fluence rate [photons/ mm^2/s] that a perfect fluoroscopy system would use to give the spatiotemporal NPS observed in the stack of frames

$$NEQ_{xyt}(f_x, f_y, f_t) = \bar{q}^2 \cdot \frac{MTF_{sys,xy}^2(f_x, f_y) \cdot MTF_t^2(f_t)}{NPS_{q,xyt}(f_x, f_y, f_t)} = \frac{IRF_{d,sys,xy}^2(f_x, f_y) \cdot MTF_t^2(f_t)}{(\Delta \bar{q}/\bar{q})^2 \cdot NPS_{d,xyt}(f_x, f_y, f_t)}. \quad (12)$$

The NEQ at the grid input, derived from equations (5), (11) and (12), is the mean photon fluence rate at the grid input ($\dot{\bar{q}}_{in}$) multiplied by $(1 - SF_{in})^2$

$$NEQ_{in,xyt} = \bar{q}_{in}^2 \cdot \frac{MTF_{in,sys,xy}^2}{NPS_{in,q,xyt}} = (1 - SF_{in})^2 \cdot \dot{\bar{q}}_{in}. \quad (13)$$

The spatiotemporal system DQE, noted $DQE_{sys,xyt}$, is the ratio between NEQ_{xyt} in the output image (equation (12)) and at the grid input (equation (13))

$$DQE_{sys,xyt}(f_x, f_y, f_t) = \frac{IRF_{d,sys,xy}^2(f_x, f_y) \cdot MTF_t^2(f_t)}{(1 - SF_{in})^2 \cdot \dot{\bar{q}}_{in} \cdot (\Delta \bar{q}/\bar{q})^2 \cdot NPS_{d,xyt}(f_x, f_y, f_t)}. \quad (14)$$

The spatiotemporal system DQE can be expressed as the product between the spatiotemporal detector DQE (DQE_{xyt}) and the grid DQE (DQE_{grid}).

$$DQE_{sys,xyt}(f_x, f_y, f_t) = DQE_{grid} \cdot DQE_{xyt}(f_x, f_y, f_t), \quad (15)$$

where DQE_{grid} is defined by the primary transmission (T_p) and the total transmission (T_t) of the anti-scatter grid (Monnin *et al* 2017)

$$DQE_{grid} = T_p^2/T_t \quad (16)$$

$$DQE_{xyt}(f_x, f_y, f_t) = \frac{IRF_{d,xy}^2(f_x, f_y) \cdot MTF_t^2(f_t)}{\dot{\bar{q}} \cdot (\Delta \bar{q}/\bar{q})^2 \cdot NPS_{d,xyt}(f_x, f_y, f_t)} = \frac{\bar{q}^2 \cdot MTF_{xy}^2(f_x, f_y) \cdot MTF_t^2(f_t)}{\dot{\bar{q}} \cdot NPS_{q,xyt}(f_x, f_y, f_t)}. \quad (17)$$

The photon fluence rate at the detector ($\dot{\bar{q}}$) is $\dot{\bar{q}}_{in}$ multiplied by T_t

$$\dot{\bar{q}} = T_t \cdot \dot{\bar{q}}_{in}. \quad (18)$$

2.2. In-plane and temporal metrics

Spatiotemporal metrics represent 3D imaging performance but not in-plane image quality as observable on frames. Frames acquired in temporal series integrate the signal and noise powers over the temporal bandwidth of the dynamic imaging system. We therefore define in-plane spatial metrics, named ‘frame system metrics’, which are measured on temporal stacks of processed frames acquired using x-ray beams with determined scatter fractions.

The ‘frame system IRF’, noted $IRF_{d,sys,frame}$, is the spatiotemporal system IRF integrated over the temporal frequency bandwidth

$$IRF_{d,sys,frame}(f_x, f_y) = \int_{-\infty}^{\infty} IRF_{d,sys,xyt}(f_x, f_y, f_t) df_t = IRF_{d,sys,xy}(f_x, f_y) \cdot \int_{-\infty}^{\infty} MTF_t(f_t) df_t. \quad (19)$$

The ‘frame NPS’, noted NPS_{frame} , is the spatiotemporal NPS integrated over the temporal frequency bandwidth, as defined by Siewerdsen *et al* (2002)

$$NPS_{d,frame}(f_x, f_y) = \int_{-\infty}^{\infty} NPS_{d,xyt}(f_x, f_y, f_t) df_t = NPS_{d,xy}(f_x, f_y) \cdot \int_{-\infty}^{\infty} NPS_t(f_t) df_t. \quad (20)$$

The ‘temporal NPS’, noted NPS_{temp} , is the spatiotemporal NPS integrated over the spatial frequency bandwidth (Siewerdsen *et al* 2002)

$$NPS_{temp}(f_t) = \int_{-\infty}^{\infty} \int_{-\infty}^{\infty} NPS_{d,xyt}(f_x, f_y, f_t) df_x df_y = NPS_t(f_t) \cdot \int_{-\infty}^{\infty} \int_{-\infty}^{\infty} NPS_{d,xy}(f_x, f_y) df_x df_y. \quad (21)$$

The units of $NPS_{d,frame}$ and NPS_{temp} are $[mm^2]$ and $[s]$, respectively.

The ‘frame NEQ’, noted NEQ_{frame} , assesses the in-plane image quality observable in fluoroscopy frames

$$NEQ_{frame}(f_x, f_y) = \bar{q}^2 \cdot \frac{MTF_{sys,xy}^2(f_x, f_y) \cdot \int_{-\infty}^{\infty} MTF_t^2(f_t) df_t}{\int_{-\infty}^{\infty} NPS_{q,xyt}(f_x, f_y, f_t) df_t} = \frac{IRF_{d,sys,xy}^2(f_x, f_y) \cdot \int_{-\infty}^{\infty} MTF_t^2(f_t) df_t}{(\Delta\bar{q}/\bar{q})^2 \cdot \int_{-\infty}^{\infty} NPS_{d,xyt}(f_x, f_y, f_t) df_t}. \quad (22)$$

The frame NEQ represents the photon fluence rate that a perfect fluoroscopy system would have used to give the noise level observed in frames, expressed in $[photons/mm^2/s]$. The frame NEQ takes into account the power of the temporal MTF, and differs from the planar NEQ used in conventional radiography. If the temporal resolution is omitted when computing the NEQ for fluoroscopy frames, the motion blur is overlooked and only the noise level is integrated over the temporal frequency bandwidth. This omission leads to a decrease in frame NPS without any change in the MTF. This implies the worst temporal resolution will incorrectly give the higher NEQ.

The ‘frame system DQE’, noted $DQE_{sys,frame}$, assesses the in-plane imaging performance of fluoroscopy frames. It can be expressed in several equivalent formulations given in equation (23)

$$\begin{aligned} DQE_{sys,frame}(f_x, f_y) &= \frac{\bar{q}^2 \cdot MTF_{sys,xy}^2(f_x, f_y) \cdot \int_{-\infty}^{\infty} MTF_t^2(f_t) df_t}{(1 - SF_{in})^2 \cdot \dot{q}_{in} \cdot \int_{-\infty}^{\infty} NPS_{q,xyt}(f_x, f_y, f_t) df_t} \\ &= \frac{IRF_{d,sys,xy}^2(f_x, f_y) \cdot \int_{-\infty}^{\infty} MTF_t^2(f_t) df_t}{(1 - SF_{in})^2 \cdot \dot{q}_{in} \cdot (\Delta\bar{q}/\bar{q})^2 \cdot \int_{-\infty}^{\infty} NPS_{d,xyt}(f_x, f_y, f_t) df_t} \\ &= \frac{T_p^2}{T_t} \cdot \frac{IRF_{d,xy}^2(f_x, f_y) \cdot \int_{-\infty}^{\infty} MTF_t^2(f_t) df_t}{\dot{q} \cdot (\Delta\bar{q}/\bar{q})^2 \cdot \int_{-\infty}^{\infty} NPS_{d,xyt}(f_x, f_y, f_t) df_t}. \end{aligned} \quad (23)$$

Using equation (8) and the first formulation of equation (23), $DQE_{sys,frame}$ can be expressed as the product between four terms given in equation (24)

$$DQE_{sys,frame}(f_x, f_y) = \frac{T_p^2}{T_t} \cdot \frac{\bar{q} \cdot \Delta t}{NPS_{q,xyt}(0, 0, 0)} \cdot \frac{MTF_{sys,xy}^2(f_x, f_y)}{NTF_{q,xy}^2(f_x, f_y)} \cdot \frac{\int_{-\infty}^{\infty} MTF_t^2(f_t) df_t}{\int_{-\infty}^{\infty} NTF_t^2(f_t) df_t}. \quad (24)$$

The 1st term is the grid efficiency (DQE_{grid}). The 2nd term represents the spatiotemporal DQE (equation (17)) at zero frequency. The 3rd term is a fraction in the spatial frequency space, which decreases below 1.0 as a function of the decorrelation between signal and noise in the spatial frequency domain. The 4th term is a fraction of integrals in the temporal frequency domain that decreases below 1.0 as a function of the decorrelation between signal and noise in the temporal frequency domain.

When measured without scatter ($SF_{in} = 0$) and without grid ($\dot{q} = \dot{q}_{in}$ and $DQE_{grid} = 1$), $DQE_{sys,frame}$ is equal to the frame detector DQE, noted DQE_{frame} and given in equation (25)

$$DQE_{frame}(f_x, f_y) = \frac{\bar{q}^2 \cdot MTF_{xy}^2(f_x, f_y) \cdot \int_{-\infty}^{\infty} MTF_t^2(f_t) df_t}{\dot{q} \cdot \int_{-\infty}^{\infty} NPS_{q,xyt}(f_x, f_y, f_t) df_t} = \frac{IRF_{d,xy}^2(f_x, f_y) \cdot \int_{-\infty}^{\infty} MTF_t^2(f_t) df_t}{\dot{q} \cdot (\Delta\bar{q}/\bar{q})^2 \cdot \int_{-\infty}^{\infty} NPS_{d,xyt}(f_x, f_y, f_t) df_t}. \quad (25)$$

DQE_{frame} reverts to the lag-corrected DQE defined in equation (25) in Cunningham *et al* (2001) and in equation (2) in Friedman and Cunningham (2010).

2.3. System with a perfect temporal resolution

We consider the special case of a dynamic imaging system with a perfect temporal resolution determined only by the x-ray pulse length a_t , without lag and without temporal processing (i.e. without correlation between consecutive frames). The power of the temporal signal is inversely proportional to a_t

$$MTF_t(f_t) = \text{sinc}(\pi \cdot a_t \cdot f_t) \quad (26)$$

$$\int_{-\infty}^{\infty} MTF_t^2(f_t) df_t = \int_{-\infty}^{\infty} \text{sinc}^2(\pi \cdot a_t \cdot f_t) df_t \cong \frac{1}{a_t}. \quad (27)$$

The temporal component of the spatiotemporal NPS sampled along the temporal frequency axis is white

$$NPS_t(f_t) = \Delta t \cdot \sum_{k_t=-\infty}^{\infty} \text{sinc}^2\left(\pi \cdot a_t \cdot \left(f_t - \frac{k_t}{\Delta t}\right)\right) = \frac{\Delta t^2}{a_t}. \quad (28)$$

The power of the temporal component of NPS_{xyt} is the ratio $\Delta t/a_t$, equal to 1.0 for continuous fluoroscopy

$$\int_{-\infty}^{\infty} NPS_t(f_t) df_t = \int_{-\infty}^{\infty} \frac{\Delta t^2}{a_t} df_t = \frac{\Delta t^2}{a_t} \cdot 2f_{t,Nyq} = \frac{\Delta t}{a_t}. \quad (29)$$

For a given dose per frame, the frame NPS is proportional to the ratio $\Delta t/a_t$

$$NPS_{d,frame}(f_x, f_y) = \frac{\Delta t}{a_t} \cdot NPS_{d,xy}(f_x, f_y). \quad (30)$$

For a quantum limited fluoroscopy system, the frame NEQ is proportional to the dose rate at the detector \dot{q}

$$NEQ_{frame}(f_x, f_y) = \frac{\bar{q}^2 \cdot MTF_{sys,xy}^2(f_x, f_y)}{\Delta t \cdot NPS_{q,xy}(f_x, f_y)} = \frac{\bar{q} \cdot MTF_{sys,xy}^2(f_x, f_y)}{NPS_{q,xy}(f_x, f_y)} \cdot \dot{q}. \quad (31)$$

The frame system DQE is independent of any temporal parameter

$$DQE_{sys,frame}(f_x, f_y) = \frac{T_p^2}{T_t} \cdot \frac{\bar{q} \cdot MTF_{xy}^2(f_x, f_y)}{NPS_{q,xy}(f_x, f_y)}. \quad (32)$$

2.4. System with temporal resolution determined by a recursive temporal filter

We consider the special case of a dynamic imaging system with a temporal resolution determined by a recursive temporal filter. The effect of the x-ray pulse length on the temporal resolution is negligible compared to that of the temporal filter, and no aliasing of temporal signal and noise occurs. The temporal resolution of this system can be adjusted through the 'k-factor' of the recursive filter that adds consecutive frames using the scheme given in equation (33).

$$y(t) = \frac{1}{k} \cdot x(t) + \left(1 - \frac{1}{k}\right) \cdot y(t - \Delta t), \quad (33)$$

where $y(t)$ is the output image, $x(t)$ is the newly acquired image and k is the gain of the recursive filter, a constant between 1 and $+\infty$ ($k = 1$ without temporal filtering and $k = +\infty$ with an infinite temporal filtering). The transfer function of the recursive temporal filter, noted $H_t(f_t)$, is determined by the temporal frame spacing Δt and the k -factor (Wilson *et al* 1997, 1999)

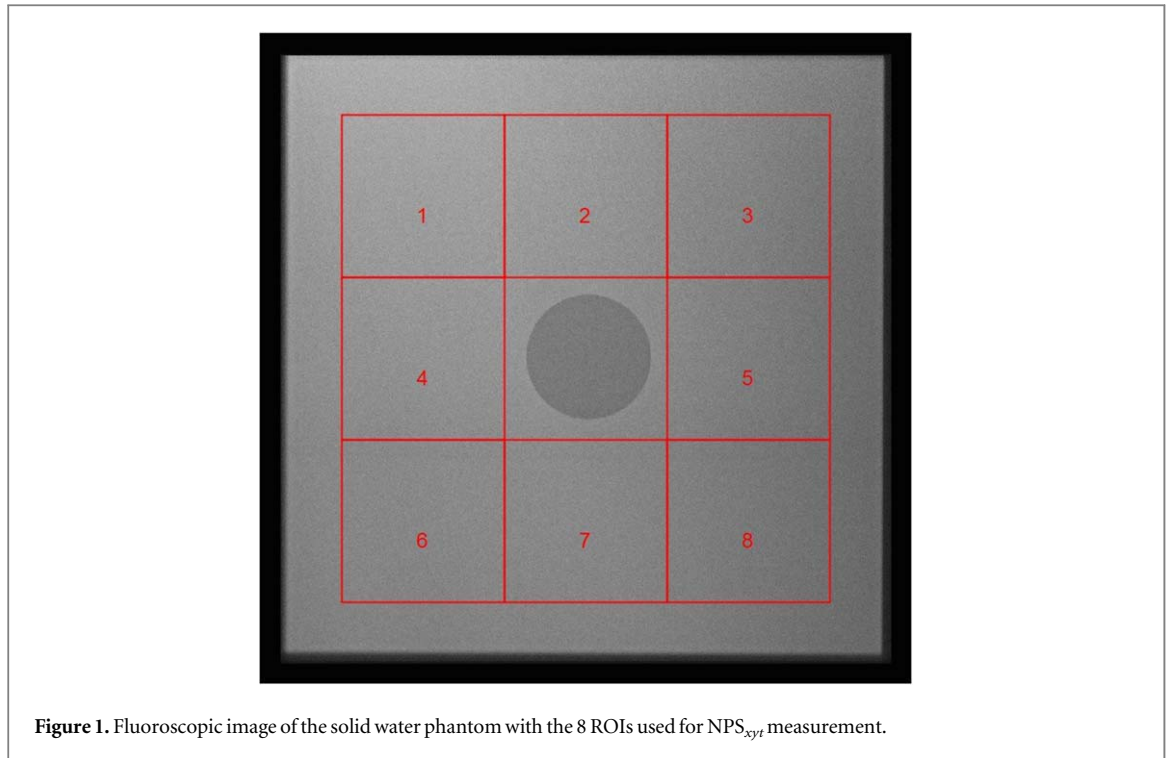
$$H_t(f_t) = \frac{1}{\sqrt{1 + 4k(k-1) \cdot \sin^2(\pi \cdot \Delta t \cdot f_t)}}. \quad (34)$$

The temporal MTF is roughly equal to the temporal filter $H_t(f_t)$

$$MTF_t(f_t) = H_t(f_t) \cdot \text{sinc}(\pi \cdot a_t \cdot f_t) \cong H_t(f_t). \quad (35)$$

Table 1. Technical parameters of the fluoroscopy systems.

	Detector type	Detector size [mm ²]	Image matrix	Pixel size [mm]	Grid $f_0/r/N$ [cm/-/mm ⁻¹]	SDD [cm]
Cios Fusion	CsI/a-Si TFT switch	200 × 200	1024 × 1024	0.194	100/17/7	102
Axiom Artis Zee	CsI/a-Si TFT switch	300 × 300	1024 × 1024	0.308	105/15/8	119

**Table 2.** X-ray beam parameters.

Beam	Solid water [mm]	Air gap [mm]	FOV [mm ²]	Grid	Voltage [kV]	Copper filtration [mm]	φ [mm ⁻² μ Gy ⁻¹]	$\Delta\bar{q}/\bar{q}$	SF_{in}
Cios Fusion									
B1^a	200	150	200 × 200	In	64	0.1	28382	0.248	0.564
B2	200	150	150 × 150	In	64	0.1	28382	0.248	0.466
B3	200	250	200 × 200	In	64	0.1	28382	0.248	0.444
Axiom Artis Zee									
B4	50	150	300 × 300	In	58	0.2	24576	0.330	0.342
B5	100	150	300 × 300	In	68	0.2	28330	0.250	0.503
B6	150	150	300 × 300	In	81	0.2	31241	0.181	0.611
B7^a	200	150	300 × 300	In	96	0.2	32167	0.134	0.694
B8	50	150	300 × 300	Out	54	0.2	23196	0.359	0.343
B9	100	150	300 × 300	Out	62	0.2	26820	0.281	0.502
B10	150	150	300 × 300	Out	71	0.2	29870	0.216	0.607
B11	200	150	300 × 300	Out	83	0.2	31974	0.162	0.693

^a Reference configuration for each system.

The integral of MTF_t^2 is determined by the k -factor of the temporal recursive filter and Δt

$$\int_{-\infty}^{\infty} MTF_t^2(f_t) df_t \cong \int_{-\infty}^{\infty} H_t^2(f_t) df_t = \frac{1}{(2k-1) \cdot \Delta t}. \quad (36)$$

The temporal component of the spatiotemporal NPS is determined by Δt and $H_t(f_t)$

$$NPS_t(f_t) = \Delta t \cdot H_t^2(f_t) \cdot \text{sinc}^2(\pi \cdot a_t \cdot f_t) \cong \Delta t \cdot H_t^2(f_t) = \frac{\Delta t}{1 + 4k(k-1) \cdot \sin^2(\pi \cdot \Delta t \cdot f_t)}. \quad (37)$$

The integral of NPS_t depends only on the k -factor of the temporal recursive filter

$$\int_{-\infty}^{\infty} NPS_t(f_t) df_t = \Delta t \cdot \int_{-\infty}^{\infty} H_t^2(f_t) df_t = \frac{1}{2k-1}. \quad (38)$$

Table 3. Dosimetric parameters.

Beam	fps	Current [mA]	Pulse width [ms]	\dot{K}_{in} [uGy.min ⁻¹]	$K_{in}/frame$ [nGy]	\dot{q}_{in} [mm ⁻² s ⁻¹]
Cios Fusion						
B1	3	24.2	14.6	10.2	57	4 819
B1	5	24.1	12.6	16.6	56	7 865
B1	10	23.7	12.1	32.7	55	15 458
B1	15	23.6	11.0	46.9	52	22 188
B1	30	5.5	33.3	85.5	47	40 465
B2	15	23.6	11.0	44.5	49	21 051
B3	15	23.6	11.0	35.3	39	16 686
Axiom Artis Zee						
B4	15	13.0	3.6	57.3	62	23 469
B5	15	13.0	3.6	53.6	60	25 304
B6	15	13.0	3.6	50.7	55	26 420
B7	3	13.0	3.6	10.5	61	5 655
B7	7.5	13.0	3.6	25.8	58	13 856
B7	15	13.0	3.6	50.7	58	27 204
B7	30	13.0	3.6	103.8	57	55 629
B8	15	13.0	3.6	36.1	40	13 960
B9	15	13.0	3.6	30.4	33	13 592
B10	15	13.0	3.6	26.8	30	13 340
B11	15	13.0	3.6	25.3	28	13 469

Table 4. Image processing.

Parameter	Cios Fusion		Axiom Artis Zee	
	Default value	Other tested values	Default value	Other tested values
Digital density optimization (DDO)	On	—	25%	—
Edge enhancement	Off	Low, high	Off	50%
Noise reduction/i-noise	Off	Low, high	Off	Liss
Temporal filter/k-factor	Off	Low, high	$k = 2.5$	$k = 1.0, 1.6, 5.0, 8.0$
Motion detection with active noise reduction	Off	—	Off	—
Metal correction	Off	—	Off	—

For a given dose per frame, the frame NPS is inversely proportional to $(2k - 1)$

$$NPS_{d,frame}(f_x, f_y) = \frac{1}{2k - 1} \cdot NPS_{d,xy}(f_x, f_y). \quad (39)$$

Because the recursive temporal filter does not decorrelate NPS_t from MTF_t^2 , the frame NEQ and frame system DQE both revert to the case of perfect temporal resolution (equations (31) and (32), respectively).

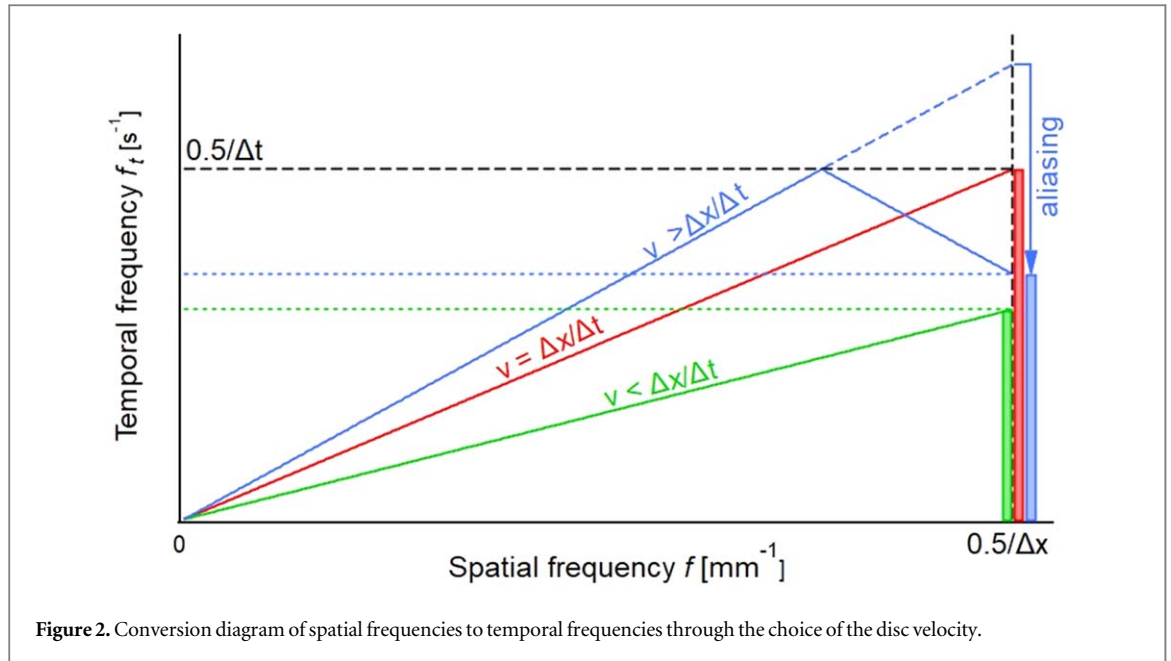
3. Material and methods

3.1. Experimental set-up

Two flat panel fluoroscopy systems were involved in this study: a C-arm Cios Fusion and a floor-mounted cardiology Axiom Artis Zee (Siemens Healthcare, Forchheim, Germany). The technical characteristics of the fluoroscopy systems are given in table 1.

Solid water (SW) plates of $30 \times 30 \text{ cm}^2$ were used to mimic four different patient thicknesses (50, 100, 150 and 200 mm). A sharp-edged 50 mm (0.1 mm thick) copper disc was positioned on top and at the middle of the SW phantom (figure 1). The images of the SW phantom were acquired in the high quality mode FL + using the tube voltage, tube current, x-ray pulse length and additional copper filter chosen by the AERC settings. The different SW phantom thicknesses generated automatic variations of the tube current (mA), pulse width and voltage (kV) that produced different x-ray beam qualities and SF_{in} (tables 2 and 3).

As reference imaging conditions, we chose the maximal FOV ($200 \times 200 \text{ mm}^2$ for the Cios Fusion and $300 \times 300 \text{ mm}^2$ for the Axiom Artis Zee), an air gap of 150 mm between the phantom and the anti-scatter grid, and the default image processing applied by the systems (table 4). Different geometrical and technical



configurations were tested and led to eleven x-ray energy spectra (beams numbered B1–B11 detailed in table 2). The impact of the grid was investigated for the four phantom thicknesses on the Axiom Artis Zee (beams B8–B11 with the anti-scatter grid removed). Different frame rates from 3 to 30 fps (table 3) and different strengths of spatial and temporal image processing (table 4) were also tested in the reference conditions.

3.2. Dosimetry

The reference plane for all dosimetric quantities is the detector (image) plane. X-ray spectra computed using the method described in Boone and Seibert (1997) gave the fluence of photons per unit exposure of the x-ray beams B1–B11 (φ in table 2) and the relative radiant contrast of the 0.1 mm sharp-edged copper disc ($\Delta\bar{q}/\bar{q}$ in table 2). A RaySafe X2 dosimeter (Unfors RaySafe AB, Billdal, Sweden) with the R/F sensor positioned at the middle of the FOV on the anti-scatter grid cover was used to measure the input air kerma rate (primary and scattered radiation at the grid input plane). The air kerma rate measured at the grid input was corrected by an inverse square law for the distance to obtain the input air kerma rate at the detector plane (\dot{K}_{in} in table 3). The product of \dot{K}_{in} with the photon fluence per air kerma unit φ gave the input photon fluence rate at the detector \dot{q}_{in}

$$\dot{q}_{in} = \varphi \cdot \dot{K}_{in}. \quad (40)$$

The values \dot{K}_{in} and \dot{q}_{in} represent the rate of air kerma and photon fluence that would be at the detector without the anti-scatter grid. No correction was made for the transmission of the carbon fibre cover of the detector housing. Table 3 summarizes the dosimetric parameters obtained for the different configurations.

3.3. Scatter fraction at the system input

The scatter fraction at system input (SF_{in}) is the SF produced by the SW phantom at the anti-scatter grid input plane. The measurement of SF_{in} is needed for the calculation of the system DQE only. This requires the determination of the response of the imaging system to detector air kerma (DAK) on pre-processed images. Most of fluoroscopy systems do not provide access to pre-processed images and to manual settings of the tube voltage (kV) and current time product (mAs). SF_{in} was therefore determined on ‘For processing’ images in a Dicom format acquired on a radiography system using an x-ray flat panel detector (PaxScan 4336 W, Varian Medical Systems, Palo Alto, CA, U.S.). SF_{in} mainly depends on the SW phantom characteristics (thickness and material), tube voltage, x-ray beam collimation and geometry of the x-ray imaging system (Smith and Kruger 1986, Boone and Seibert 1988). The inherent aluminium filtration of the x-ray tube plays only a marginal role and the target angle is not considered as an influencing parameter. We used x-ray tubes with the same total aluminium filtration (2.5 mm Al) and assumed that differences in off-focal radiations were negligible sources of variations in SF_{in} . The following parameters used on fluoroscopy systems were therefore reported on the radiography system to achieve the SF_{in} specific to the beams B1–B11:

- the SW phantom thicknesses
- the x-ray beam collimations at the centre of the phantom

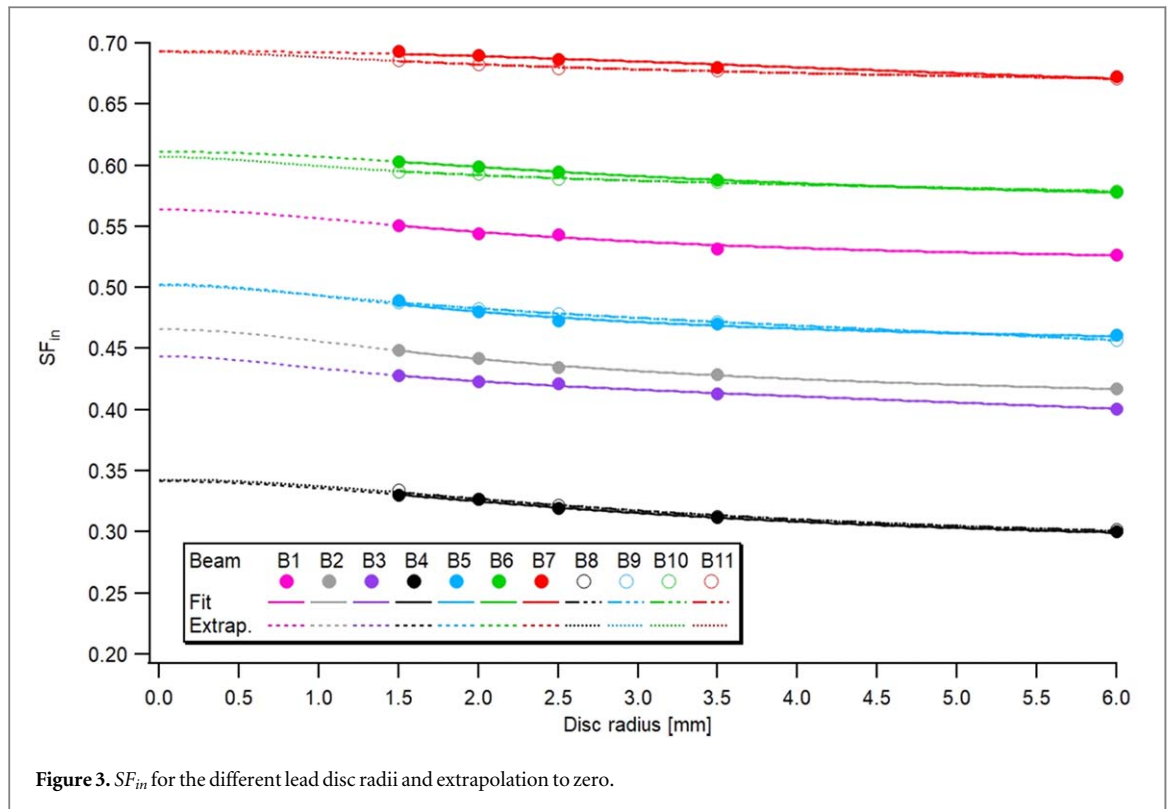


Figure 3. SF_{in} for the different lead disc radii and extrapolation to zero.

- (c) the source-to-phantom and source-to-detector distances
- (d) the tube voltages and additional copper filters.

The computation steps of the beam stop method used to determine SF_{in} are depicted in Monnin *et al* (2017). Lead blocker discs of different radii (1.5, 2, 2.5, 3.5 and 6 mm) positioned in the centre of the x-ray beam on the entrance surface of the SW phantom were imaged. An additional image without lead disc was acquired. A circular ROI with an area of 5 mm^2 positioned in the centre of the lead discs gave the mean pixel values (PV). The PV converted into DAK values using detector response functions gave the scatter as a function of the disc radius R , noted $PV(R)$. The ratio $PV(R)/PV(0)$ gave SF_{in} as a function of R . An adjustment function based on equation (41) was fitted to the measured data, where a , k_1 and k_2 are fitted coefficients

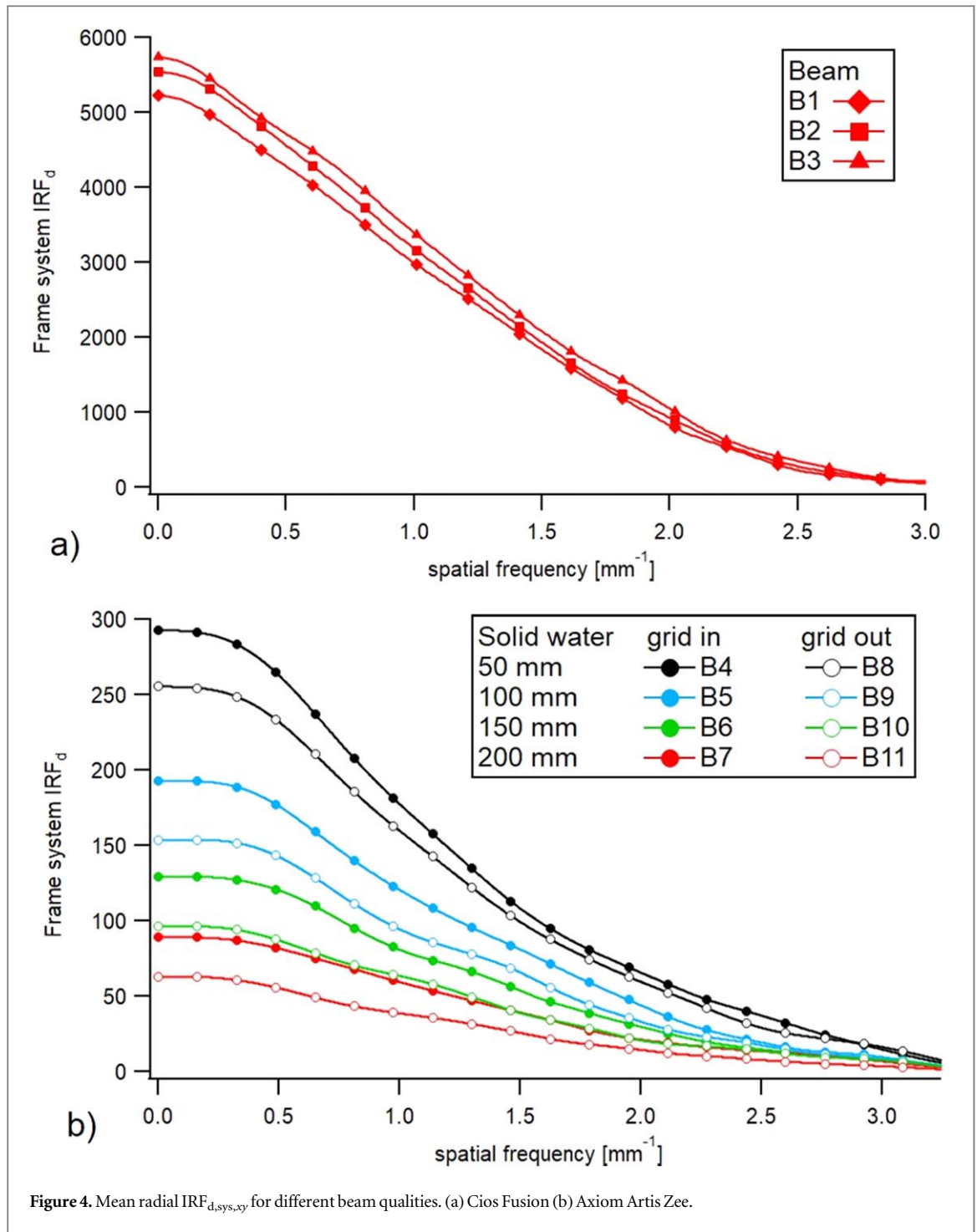
$$\frac{PV(R)}{PV(0)} = \frac{SF_{in}}{ak_1^2 + (1-a)k_2^2} \cdot \left(\frac{ak_1^2}{(1 + (R/k_1)^2)^{1/2}} + \frac{(1-a)k_2^2}{(1 + (R/k_2)^2)^{1/2}} \right). \quad (41)$$

The extrapolation of equation (41) to a disc radius zero gave SF_{in} (equation (42))

$$\lim_{R \rightarrow 0} \frac{PV(R)}{PV(0)} = SF_{in}. \quad (42)$$

3.4. Frame system IRF and MTF

A 50 mm in diameter, 0.1 mm thick sharp-edged copper disc fixed on top at the middle of the SW phantom (figure 1) was used to measure $IRF_{d,sys,frame}$. The IRF calculation is derived from the sharp edge method reported in Samei *et al* (1998). The calculation steps specific to radial coordinates are detailed in Monnin *et al* (2016). In order to increase the signal-to-noise ratio and thus the accuracy of the calculation, the computation used 500 consecutive identical images of the phantom acquired in the steady state regime of the AERC. A square ROI of $90 \times 90 \text{ mm}^2$ was centred on the disc, subdivided into 144 angular sectors of 5° aperture with an angular pitch of 2.5° . Radial profiles drawn for each angular sector from the disc centre across the edges of the disc gave 144 radial ESF over 360° . The magnitude of the 1D Fourier transform of the 144 radial ESFs gave 144 radial presampling IRFs. The mean radial $IRF_{d,sys,frame}$ is the average of the 144 resulting radial IRFs. In order to determine the NEQ and DQE in the reference plane of the detector, all IRFs were corrected for the geometrical magnification factor, determined as the ratio between the disc diameter measured on the images and the physical diameter of the disc (50 mm). The in-plane system MTF ($MTF_{sys,xy}$) is $IRF_{d,sys,frame}$ normalized to 1.0 at zero frequency.



3.5. Temporal MTF

The measurement method used in this study derives from the ‘moving slanted edge’ method described by Friedman and Cunningham (2006, 2009). The method was adapted to the radial coordinates of the sharp-edged copper disc as described in section 3.4. The copper disc used for IRF_{d,sys,frame} measurement was taped to the thin carbon plate (1 mm thick) of a motorized mobile bench placed on top of the SW phantom, and moved in a uniform rectilinear motion at a controlled speed v . The disc moving at a constant speed across the image plane generates a spatiotemporal impulse signal whose temporal frequency f_t is proportional to the spatial frequency f and speed v

$$f_t = v \cdot f = v \cdot |\cos \alpha \cdot f_x + \sin \alpha \cdot f_y|. \quad (43)$$

The angle α of the disc path was determined from linear fits to the x - and y -coordinates of the disc position on the images plotted as a function of time. IRF_{d,sys,frame} was at first measured in the frames for the disc moving at a constant speed v (equation (44)), and then without disc motion (equation (45)).

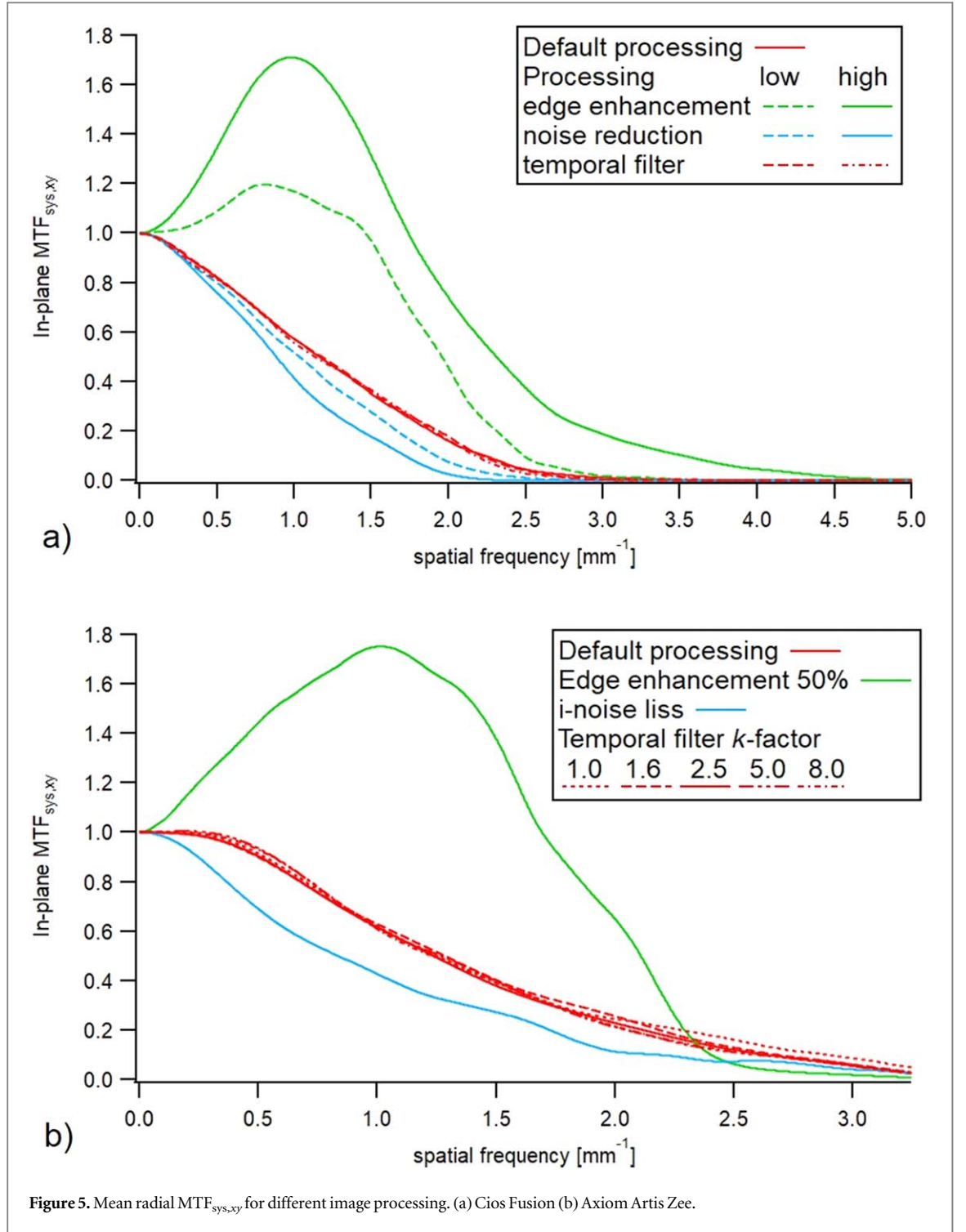


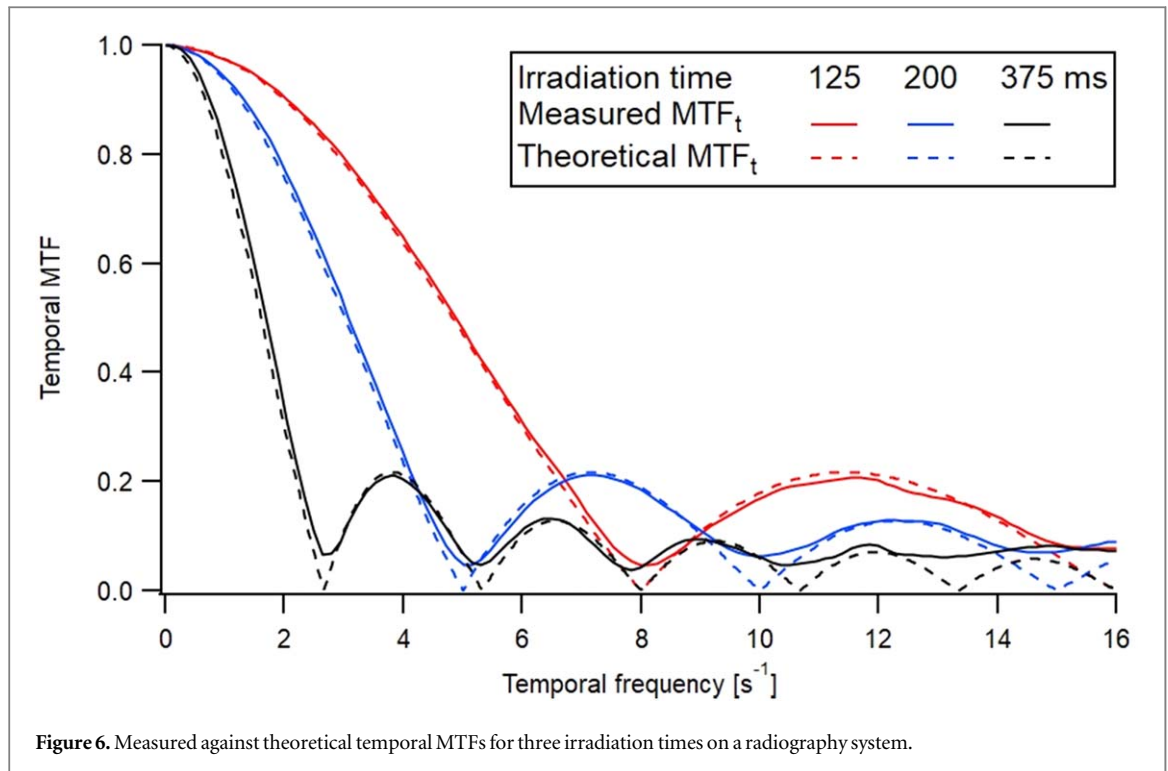
Figure 5. Mean radial MTF_{sys,xy} for different image processing. (a) Cios Fusion (b) Axiom Artis Zee.

$$IRF_{d,sys,frame}(f_x, f_y)|_{v>0} = \int_{-\infty}^{\infty} IRF_{d,sys,xyt}(f_x, f_y, f_t) df_t \Big|_{f_t=vf} = IRF_{d,sys,xy}(f_x, f_y) \cdot MTF_t(vf) \quad (44)$$

$$IRF_{d,sys,frame}(f_x, f_y)|_{v=0} = IRF_{d,sys,xy}(f_x, f_y) \cdot MTF_t(0) = IRF_{d,sys,xy}(f_x, f_y). \quad (45)$$

The static case in equation (45) gives the in-plane spatial resolution of the imaging system described in paragraph 3.4. The disc motion blurs the image of the disc according to the speed and direction of motion (Dehairs *et al* 2017). The decrease in $IRF_{d,sys,frame}$ is therefore maximum in the direction of motion and zero in the orthogonal direction. The temporal MTF is equal to the ratio between $IRF_{d,sys,frame}$ measured with and without disc motion

$$MTF_t(vf) = \frac{IRF_{d,sys,frame}(f_x, f_y)|_{v>0}}{IRF_{d,sys,frame}(f_x, f_y)|_{v=0}}. \quad (46)$$



MTF_t was finally rescaled from 2D spatial frequency coordinates to temporal frequency coordinates using equation (43). The choice of the disc velocity determines the temporal frequency range available for the calculation of MTF_t ($f_t = vf$). The disc velocity must be sufficiently high to cover the whole temporal frequency bandwidth of MTF_p, while sufficiently low to avoid aliasing artifacts in the images that could jeopardize MTF calculation. The maximal temporal frequency at which MTF_t can be measured in the image plane is limited by the spatial Nyquist frequency of the frames determined by the pixel spacing Δx (figure 2)

$$f_{t,Nyq} = v \cdot f_{x,Nyq} \Leftrightarrow \frac{0.5}{\Delta t} = v \cdot \frac{0.5}{\Delta x}. \quad (47)$$

The disc velocity used for MTF_t measurements in this study was therefore the ratio between pixel spacing Δx and frame temporal spacing Δt

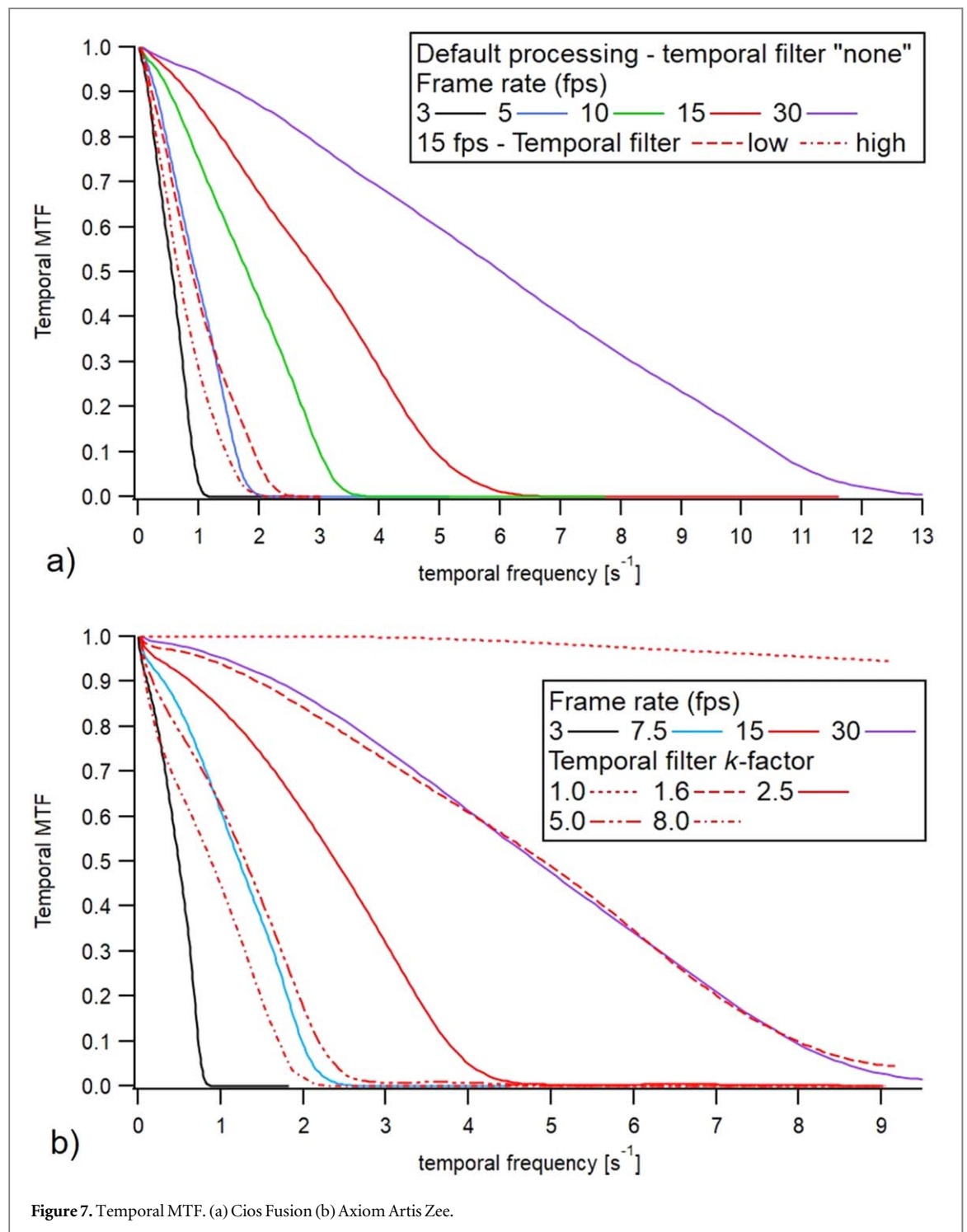
$$v = \frac{\Delta x}{\Delta t}. \quad (48)$$

Velocities lower than $\Delta x/\Delta t$ crop the temporal frequency bandwidth of the calculated temporal MTF. Velocities higher than $\Delta x/\Delta t$ give ghost images of the disc due to temporal undersampling, and consequently artefact the calculation of the temporal MTF.

To validate the computation method, MTF_t was measured on x-ray images of the copper disc acquired on a conventional radiography system using a flat panel detector (Varian PaxScan 4336 W, Varian Medical Systems, Palo Alto, CA, U.S.) whose temporal resolution is determined by the x-ray pulse length, as described in section 2.3. The computed MTF_t were compared to theoretical MTF_t given in equation (26) for the three exposure times 125, 200 and 375 ms.

3.6. Noise power spectra (NPS)

The spatiotemporal NPS was computed in the homogeneous volume of the SW phantom around the copper disc. For each imaging protocol, the 3D spatiotemporal NPS was calculated from 500 consecutive frames acquired in the steady state regime of the AERC. Each NPS was measured from eight homogeneous, consecutive and non-overlapping volumes of interest (VOIs) of $256 \times 256 \times 500$ voxels placed around the copper disc in the homogeneous SW volume of the phantom (figure 1). The 3D spatiotemporal NPS of a given VOI is the magnitude squared of the 3D Fourier transform of each VOI, calculated using equation (6) with the pixel values $d(x, y, t)$ of the processed images. No detrending correction was applied to subtract large inhomogeneities from the VOIs before NPS computation. The frame and temporal NPS were obtained by integrating NPS_{xyt} over the temporal and spatial frequency bandwidths, respectively, as shown in equations (20) and (21). The 1D radial frame NPS is the 2D frame NPS averaged over 360° , excluding the 0° and 90° axial values.

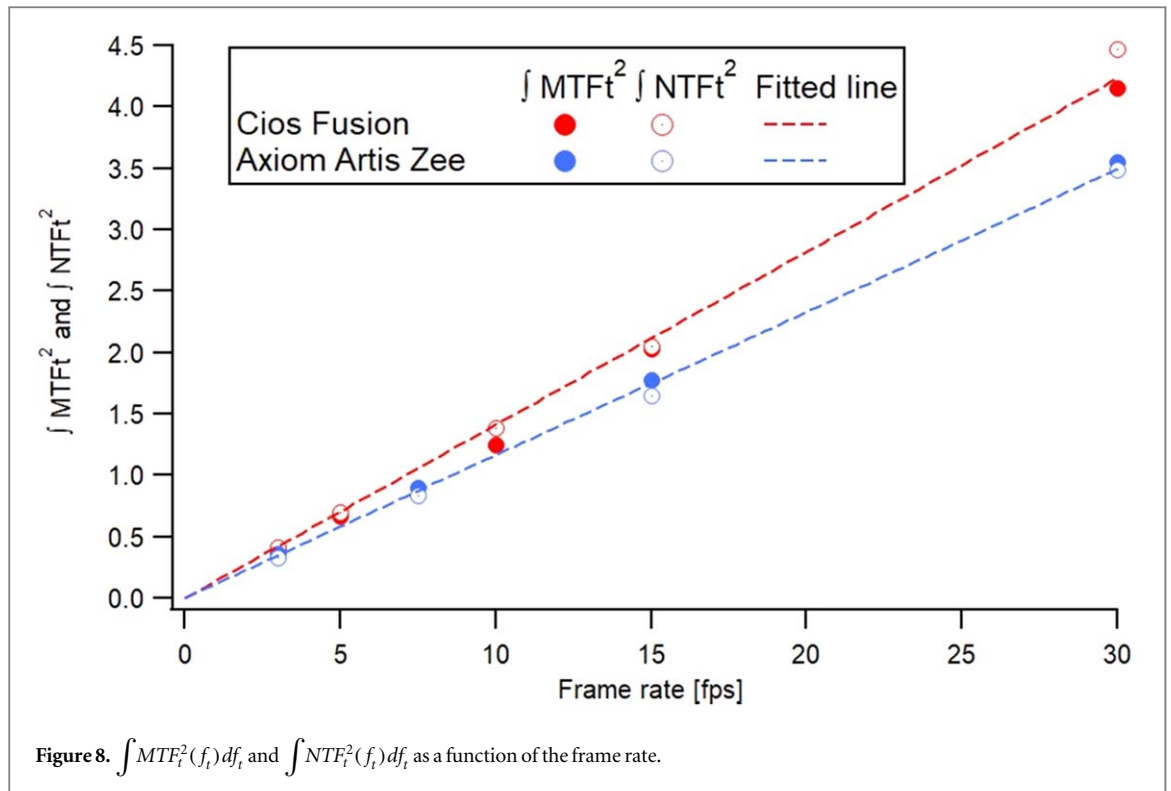


4. Results and discussion

4.1. Dosimetry and SF_{in}

The fitted curves and the extrapolations to zero of the beam stop method used to obtain SF_{in} are shown in figure 3 for the beams B1–B11 reported in table 2. Both SF_{in} and the automatic tube voltage selection increased with the phantom thickness (table 2). The results confirm that, as expected, SF_{in} increases for larger FOV and decreases with a thicker air gap between the phantom and the grid.

For a given geometrical and technical configuration, \dot{K}_{in} was proportional to the frame rate, from 10.5 $\mu\text{Gy min}^{-1}$ at 3 fps to 103.8 $\mu\text{Gy min}^{-1}$ at 30 fps (table 3). As illustrated by the data in table 3, the AERC modality controls the dose per frame and adapts to the attenuation characteristics of the phantom thickness. The air kerma per frame ($K_{in}/frame$) ranged from 28 to 62 nGy, depending on the SW phantom thickness, the air



gap and the use of the anti-scatter grid. The use of the anti-scatter grid increased the automatic adjust tube voltage and \dot{K}_{in} by a factor 1.59–2.00 on the Axiom Artis Zee for the SW thickness of 5–20 cm.

4.2. Frame system IRF and MTF

$IRF_{d,sys,frame}$ decreased when the SF at the detector increased, i.e. when the SW thickness or FOV increased, or when the air gap decreased (figure 4). For the same reason, $IRF_{d,sys,frame}$ was higher when the grid was used. The Nyquist frequencies of the Cios Fusion and Axiom Artis Zee images were 2.58 mm^{-1} and 1.62 mm^{-1} , respectively. $MTF_{sys,xy}$ dropped to zero at the Nyquist frequency for the Cios Fusion, and beyond the Nyquist frequency to around 2.7 mm^{-1} for the Axiom Artis Zee. As expected, the noise reduction (low-pass) filter decreased the in-plane spatial resolution whereas edge enhancement increased the signal at middle and high frequency (figure 5). In-plane resolution of processed images is actually more determined by spatial processing than by the image pixel size. The default processing used by the systems involved in our study gave a higher spatial resolution on the Axiom Artis Zee compared to the Cios Fusion. The temporal processing did not modify $MTF_{sys,xy}$. This result confirms the independence of spatial and temporal MTFs of fluoroscopy systems. In-plane and temporal MTFs depend on different physical parameters and can be measured separately. Note that all MTFs were corrected for the geometrical magnification factor, measured at 1.18 and 1.20 for the Cios Fusion and Axiom Artis Zee systems, respectively. Geometrical magnification decreases $MTF_{sys,xy}$ with respect to the object-to-detector distance.

4.3. Temporal MTF

The temporal MTFs measured on a conventional radiography system for three exposure times (125, 200 and 375 ms) agree with the theoretical MTF_t given in equation (26) for an x-ray system with temporal resolution determined by the x-ray pulse width (figure 6). The accuracy of the measured MTF_t decreases with an increase in temporal frequency, and gives an insight on the uncertainty of MTF_t measurement. This result validated the method of measuring temporal MTF.

In our study, the x-ray pulse length varied between 3.6 and 14.6 ms for pulsed fluoroscopy, and was 33.3 ms for continuous fluoroscopy at 30 fps (table 3). Pulsed fluoroscopy corresponds to the particular case developed in section 2.4, where the short x-ray pulse length a_t has a negligible effect on MTF_t , mostly determined by the recursive filter $H_t(f_t)$. The temporal processing of fluoroscopic frames makes MTF_t depend on the frame rate ($1/\Delta t$) and the strength (k -factor) of the temporal recursive filter (figure 7). On the Cios Fusion, the chosen fluoroscopic operating mode defined the default temporal processing, whose strength could be finely adjusted according to four different levels: none, low, medium and high. The default image processing on the Cios Fusion decreased the temporal resolution even for the default value ‘none’ (table 4). As expected, the levels ‘low’ and

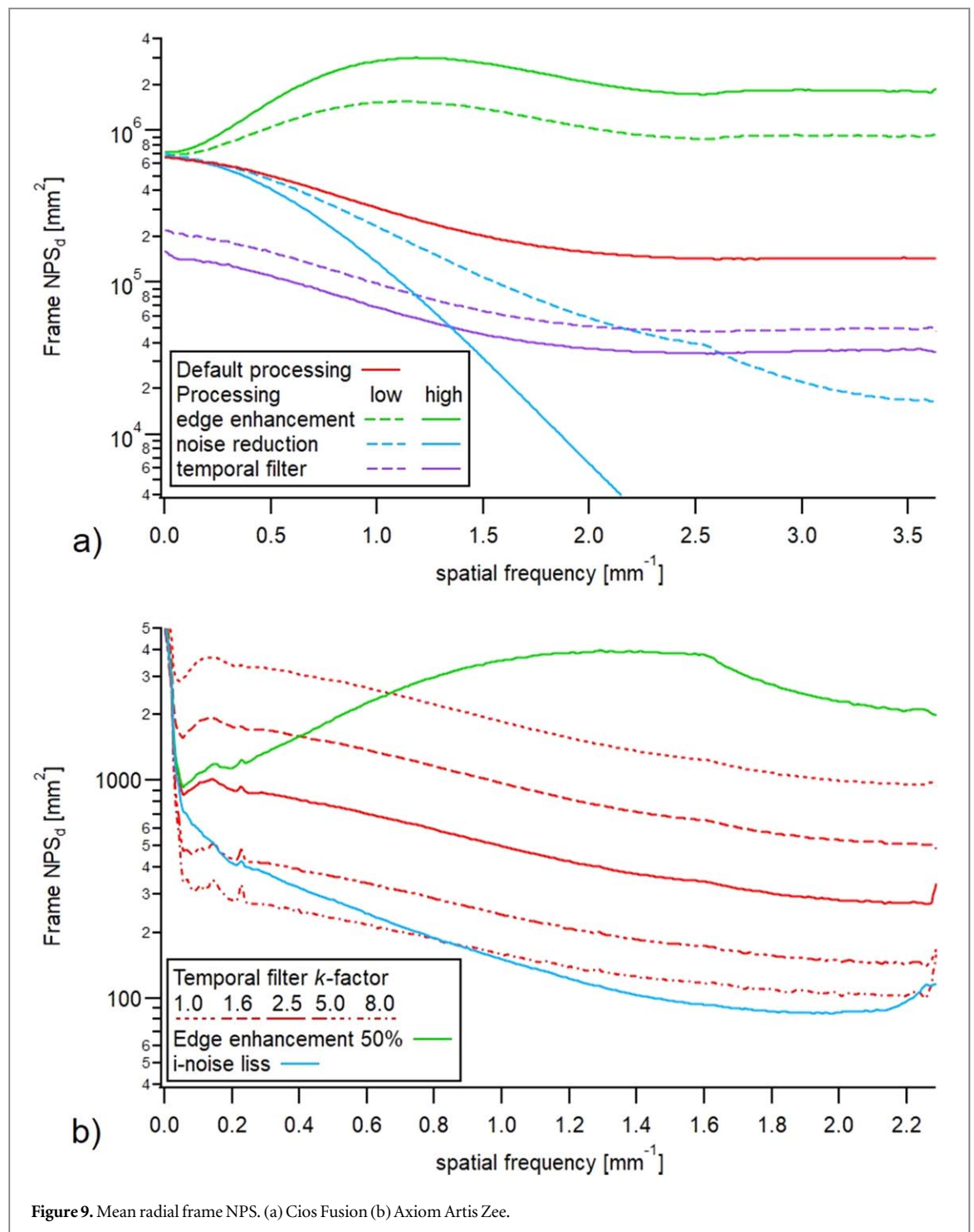


Figure 9. Mean radial frame NPS. (a) Cios Fusion (b) Axiom Artis Zee.

'high' further decreased MTF_t (figure 7(a)). On the Axiom Artis Zee system, the k -factor of the recursive temporal filter could be varied from 1.0 (none) to 8.0. MTF_t decreased when k increased from 1.0 to 8.0 (figure 7(b)). The default setting $k = 2.5$ (table 4) represents a median trade-off between image noise and temporal resolution (motion blur).

For the two fluoroscopy systems, the integral of $MTF_t^2(f_t)$ and $NTF_t^2(f_t)$ gave close proportional fits against the frame rate $1/\Delta t$, with Pearson correlation coefficients greater than 0.999 (figure 8). The default temporal processing used in this study did not decorrelate $MTF_t^2(f_t)$ from $NTF_t^2(f_t)$, both equal to $H_t^2(f_t)$. This result agrees with equation (36) and provides an indirect validation of the MTF_t calculation for the particular case with a strong correlation between consecutive frames. Note that the slope of the fitted lines is slightly higher for the Cios Fusion compared to the Axiom Artis Zee for $k = 2.5$. This means that the default temporal filter on the Cios Fusion corresponded to a k -factor smaller than 2.5.

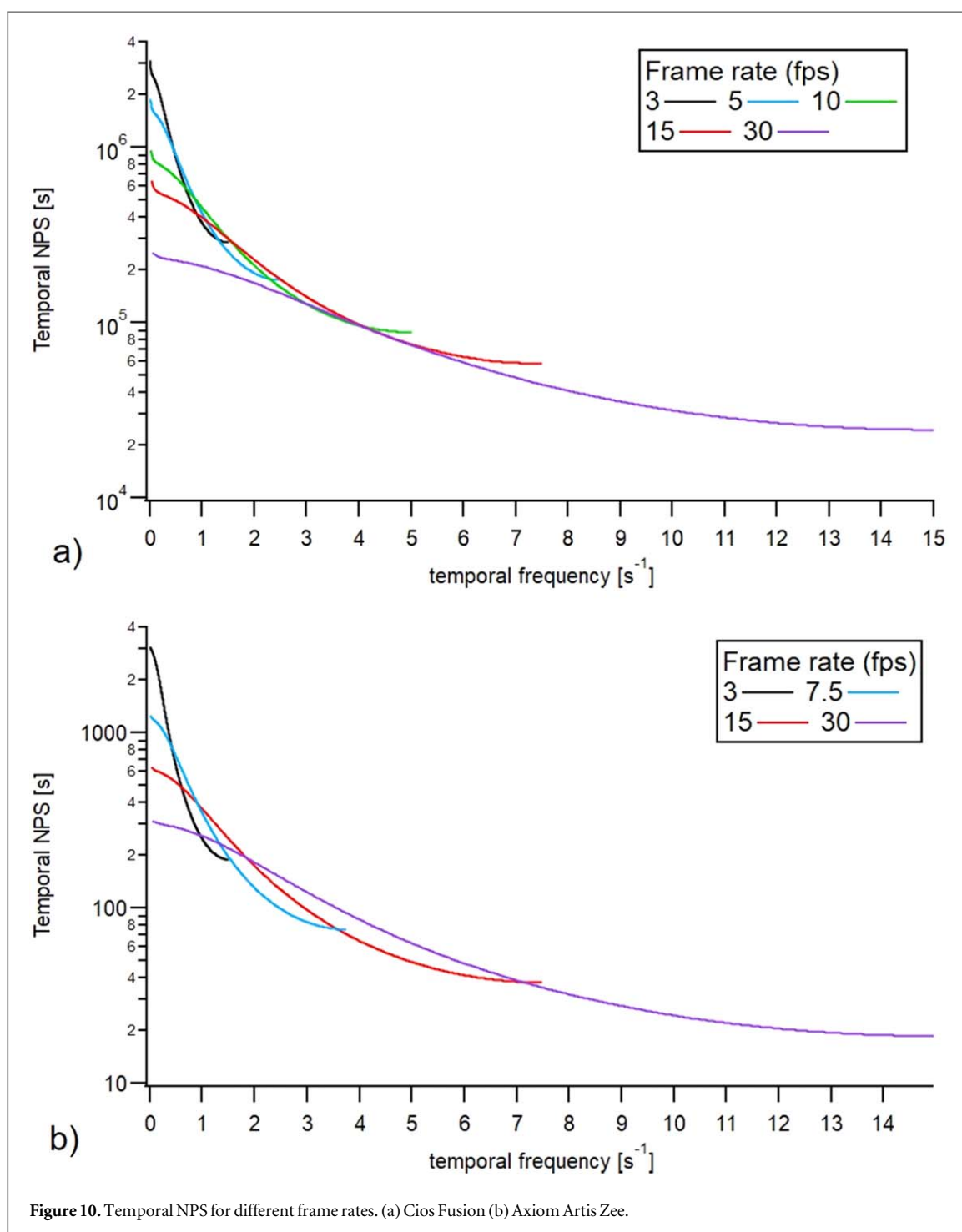


Figure 10. Temporal NPS for different frame rates. (a) Cios Fusion (b) Axiom Artis Zee.

4.4. Frame NPS

The magnitude of the frame NPS is expected to vary proportionally to the dose per frame, and to be therefore independent of the frame rate when the dose per frame is kept constant by the AERC. The frequency content of $NPS_{d,frame}$ depends on the spatial image processing, edge enhancement and noise reduction filters (figure 9). The various spatial processing demonstrate different trade-offs between spatial resolution and image noise without changing the temporal resolution. Noise reduction filters pass only low-frequency noise whereas edge enhancements give a better spatial resolution but more high-frequency noise. The magnitude of $NPS_{d,frame}$ decreased when the strength of the recursive temporal filter was increased, without changing its frequency component, in line with equation (39).

4.5. Temporal NPS

The frequency content of the temporal NPS varied with both the frame rate $1/\Delta t$ and the k -factor of the temporal recursive filter, while its zero-frequency amplitude was simply proportional to the temporal frame

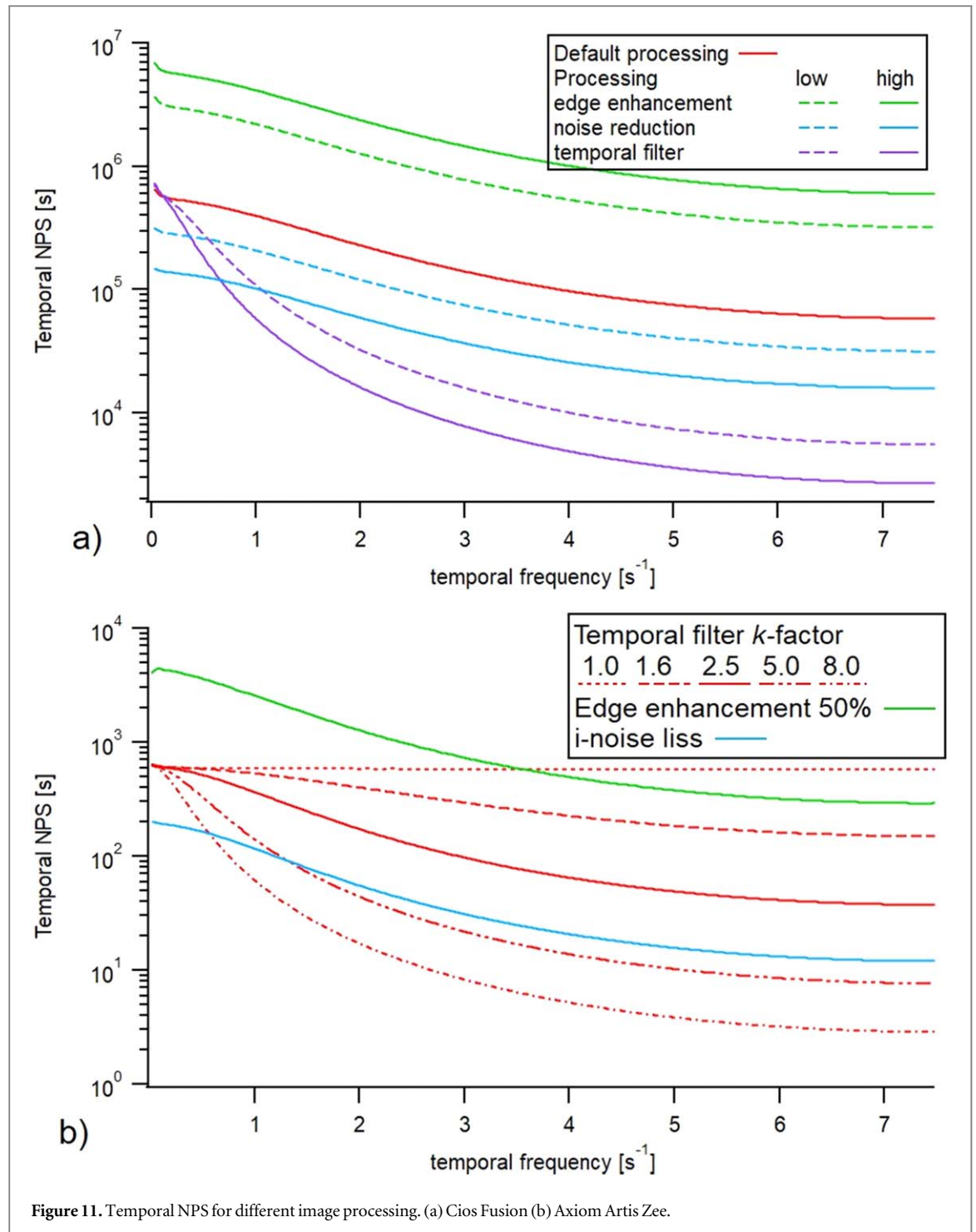
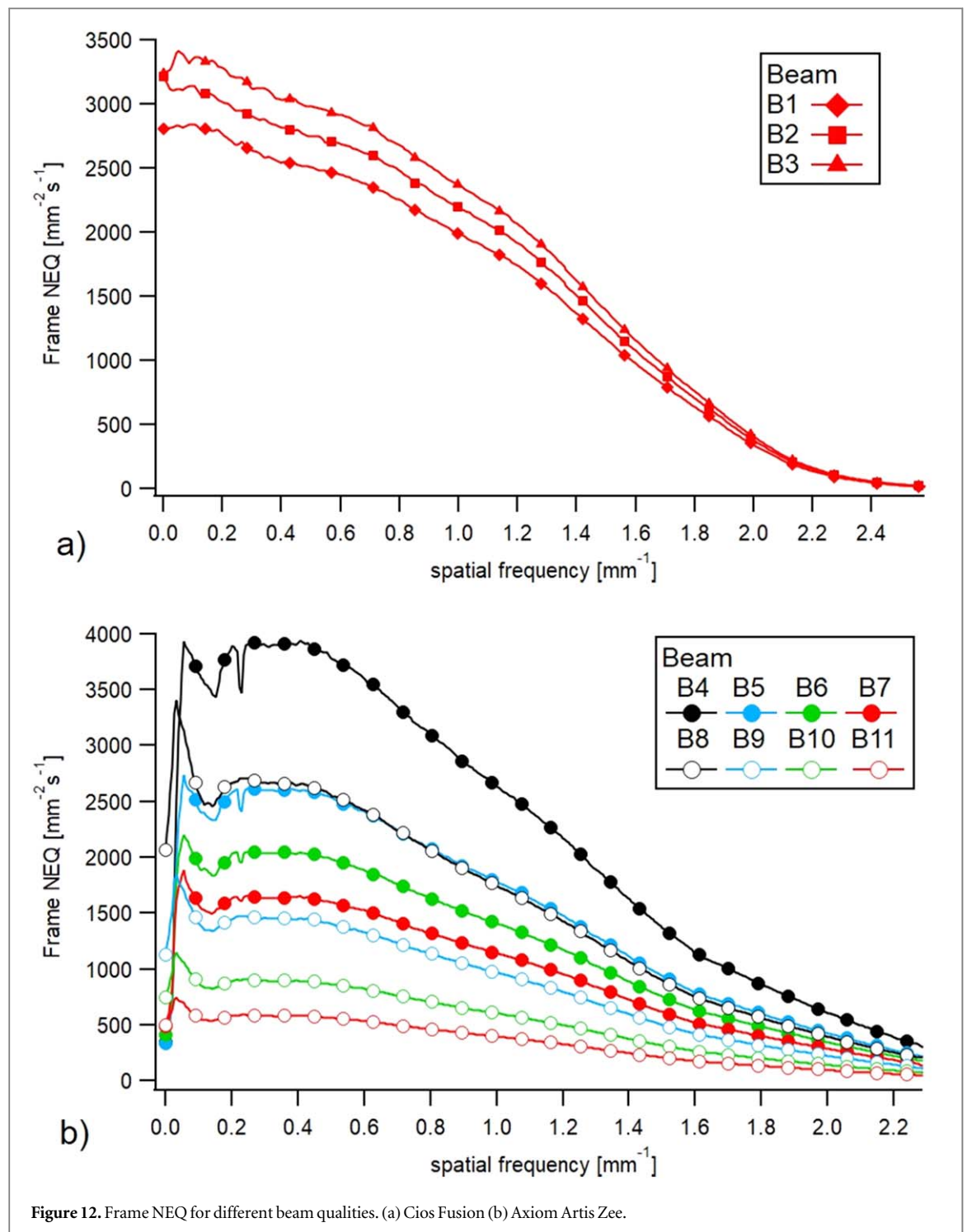


Figure 11. Temporal NPS for different image processing. (a) Cios Fusion (b) Axiom Artis Zee.

spacing, in close agreement with equation (37) (figure 10). The temporal frequency bandwidth of the temporal NPS is proportional to the frame rate while its amplitude is inversely proportional. The area under the temporal NPS curve is therefore independent of the frame rate. An increase in the recursive k -factor increased the correlation between consecutive frames and decreased the high-frequency temporal noise without changing its zero-frequency amplitude, in line with equation (37) (figure 11). Conversely, the edge enhancement and noise reduction filters respectively increased and decreased the magnitude without changing the frequency component of the temporal NPS.

4.6. Frame NEQ

NEQ_{frame} decreased when the SF at the detector (SF_{out}) increased, and was therefore higher with the anti-scatter grid than without the grid. SF_{out} increased when the SW thickness or FOV increased, or when the air gap between the SW phantom and the anti-scatter grid decreased (figure 12). NEQ_{frame} was proportional to the dose



rate at the detector, and therefore to the frame rate, as expected for fluoroscopy systems whose dose per frame is held constant by the AERC (figure 13). The ratio between MTF^2 and NPS mitigates the influence of the spatial and temporal image processing in the NEQ (figure 14). This is true only if the image processing procedures (edge enhancement and noise reduction) are linear and do not introduce different spatial correlations for the signal and the noise that would decorrelate the NPS from the MTF^2 (Bernhardt *et al* 2005, Urbanczyk *et al* 2012). For the reference conditions at 15 ips (beams B1 for the Cios Fusion and B7 for the Axiom Artis Zee), NEQ_{frame} peaks at $2800 \text{ mm}^{-2} \cdot \text{s}^{-1}$ for the Cios and around $1800 \text{ mm}^{-2} \cdot \text{s}^{-1}$ for the Axiom Artis. The Axiom Artis Zee uses higher beam energy compared to the Cios Fusion (96 kV + 0.2 mm Cu against 64 kV + 0.1 mm Cu) and 2.25 times larger FOV ($300 \times 300 \text{ mm}^2$ against $200 \times 200 \text{ mm}^2$) which produces a higher SF_{in} (0.694 against 0.564). For a similar dose rate at the grid input ($46.9 \mu\text{Gy}$ against $50.7 \mu\text{Gy}$), these differences lead to a lower grid transmission (not measured) and consequently to a lower dose rate at the detector that gives a lower NEQ_{frame} for the Axiom Artis Zee.

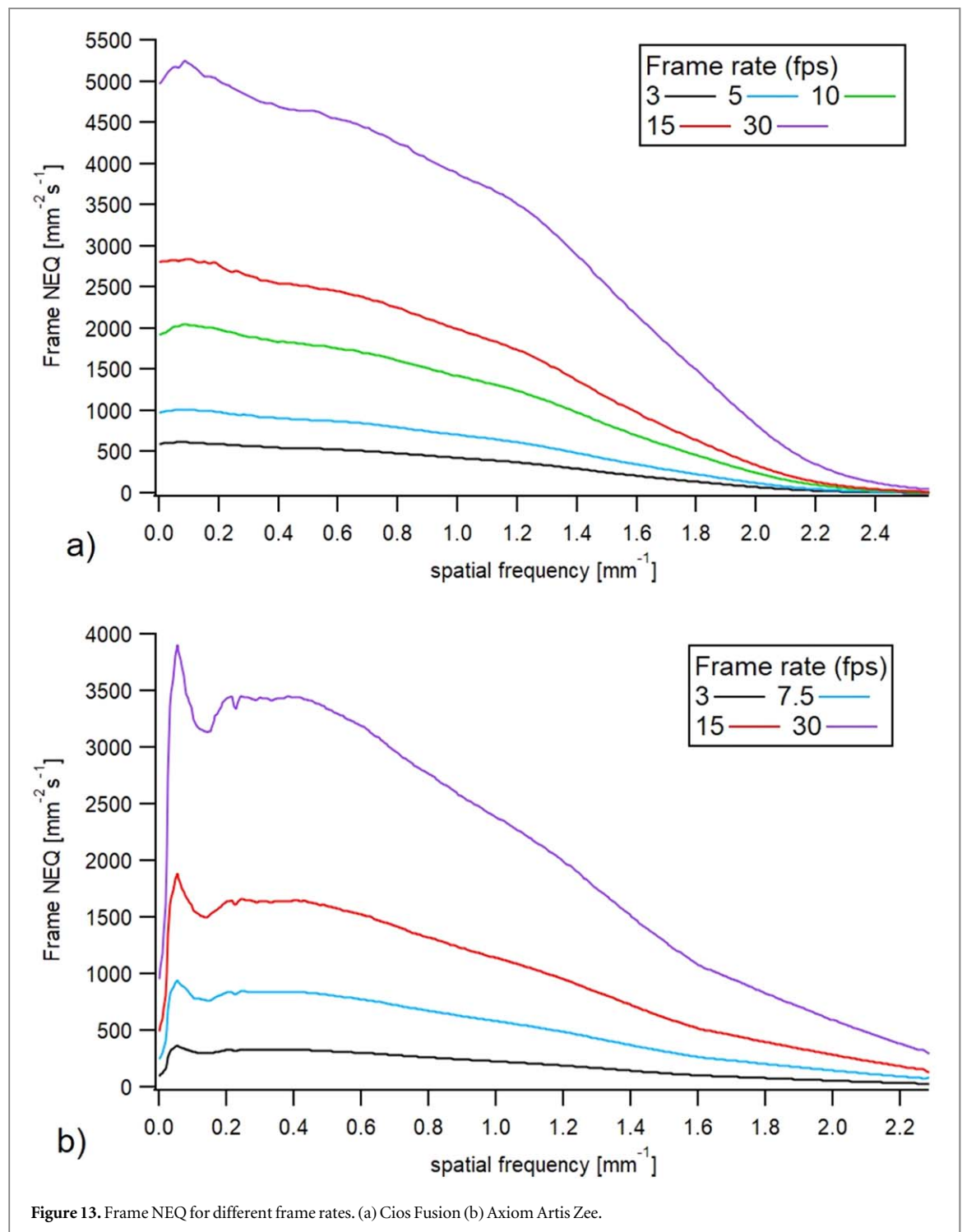
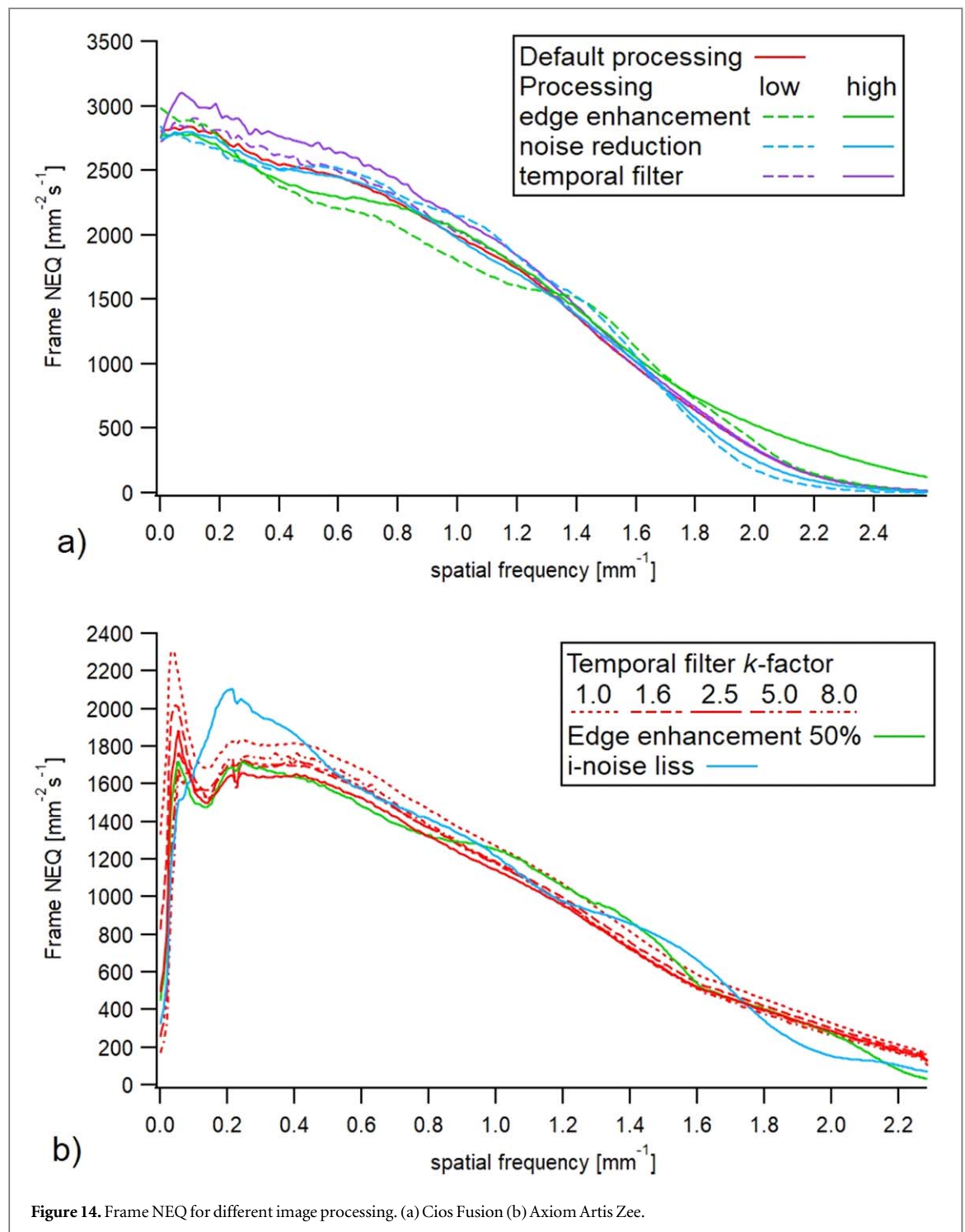


Figure 13. Frame NEQ for different frame rates. (a) Cios Fusion (b) Axiom Artis Zee.

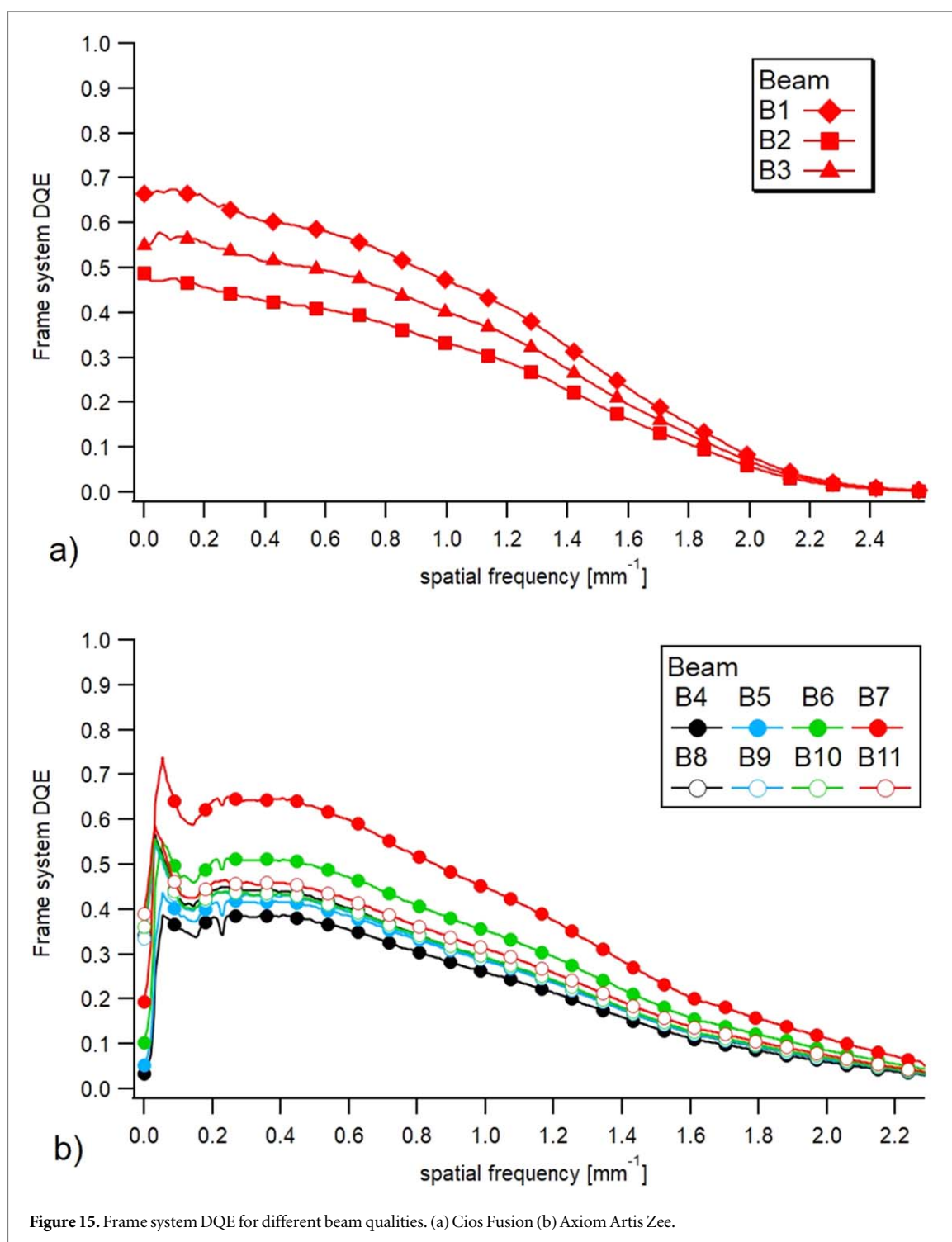
The different temporal processing strengths tested in this study on the two fluoroscopy systems did not modify NEQ_{frame} (figure 14). As shown in section 2.4, the temporal recursive filter is linear and does not decorrelate MTF_t from NPS_t . Decreasing the temporal resolution increases the correlation between pixels between consecutive frames and reduces the temporal frequency bandwidth. The frame NPS integrates the whole temporal frequency bandwidth (Siewerdsen *et al* 2002) and hence any decrease in temporal resolution reduces NPS_{frame} . This noise reduction would incorrectly inflate the NEQ and DQE if the power of MTF_t is omitted in the numerator. This happens if the NEQ and DQE are measured using a static object, ignoring the motion blur caused by the reduction in temporal resolution. This means that a simple planar formulation of the NEQ cannot be used to compare imaging performance between fluoroscopy systems with different temporal resolutions. A correction factor was therefore introduced in the NEQ and DQE formulations, based on the power of either MTF_t (Cunningham *et al* 2001, Friedman and Cunningham 2010) or NPS_t (Menser *et al* 2005). The frame NEQ proposed in this study includes the influence of MTF_t to give the actual equivalent fluence rate



of photons that an ideal fluoroscopy system would have used to give the NPS observed in the frames for the corresponding temporal resolution. NEQ_{frame} is therefore a suitable metric to compare the image quality between frames obtained with different temporal resolutions.

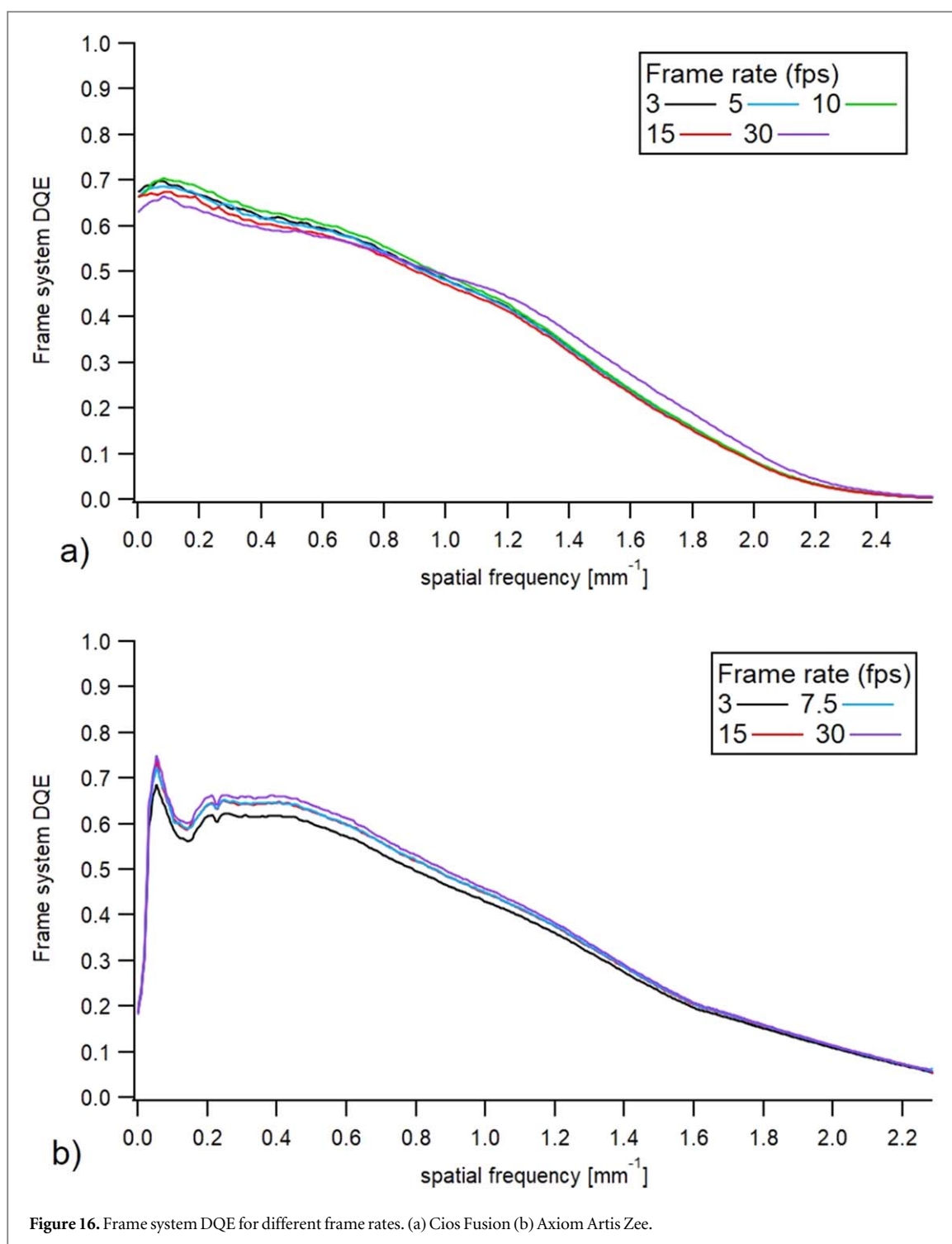
4.7. Frame system DQE

$DQE_{\text{sys,frame}}$ peaked around 0.65 for both the Cios Fusion and Axiom Artis Zee systems for 20 cm of SW with the anti-scatter grid in place (figure 15). This result shows that the two fluoroscopy systems perform equally and would thus give a comparable image quality for similar imaging conditions (phantom thickness, tube voltage, beam collimation, air gap, copper filtration, etc). The differences in image quality observed in NEQ_{frame} thus result from differences in the settings chosen by the AERC or in SF_{in} . The other SW thicknesses 5, 10 and 15 cm gave $DQE_{\text{sys,frame}}$ around 0.38, 0.42 and 0.50, respectively. Without the grid, $DQE_{\text{sys,frame}}$ was approximately equal to 0.43, regardless of the SF. The grid DQE increases with SF_{in} whereas the detector DQE is independent of



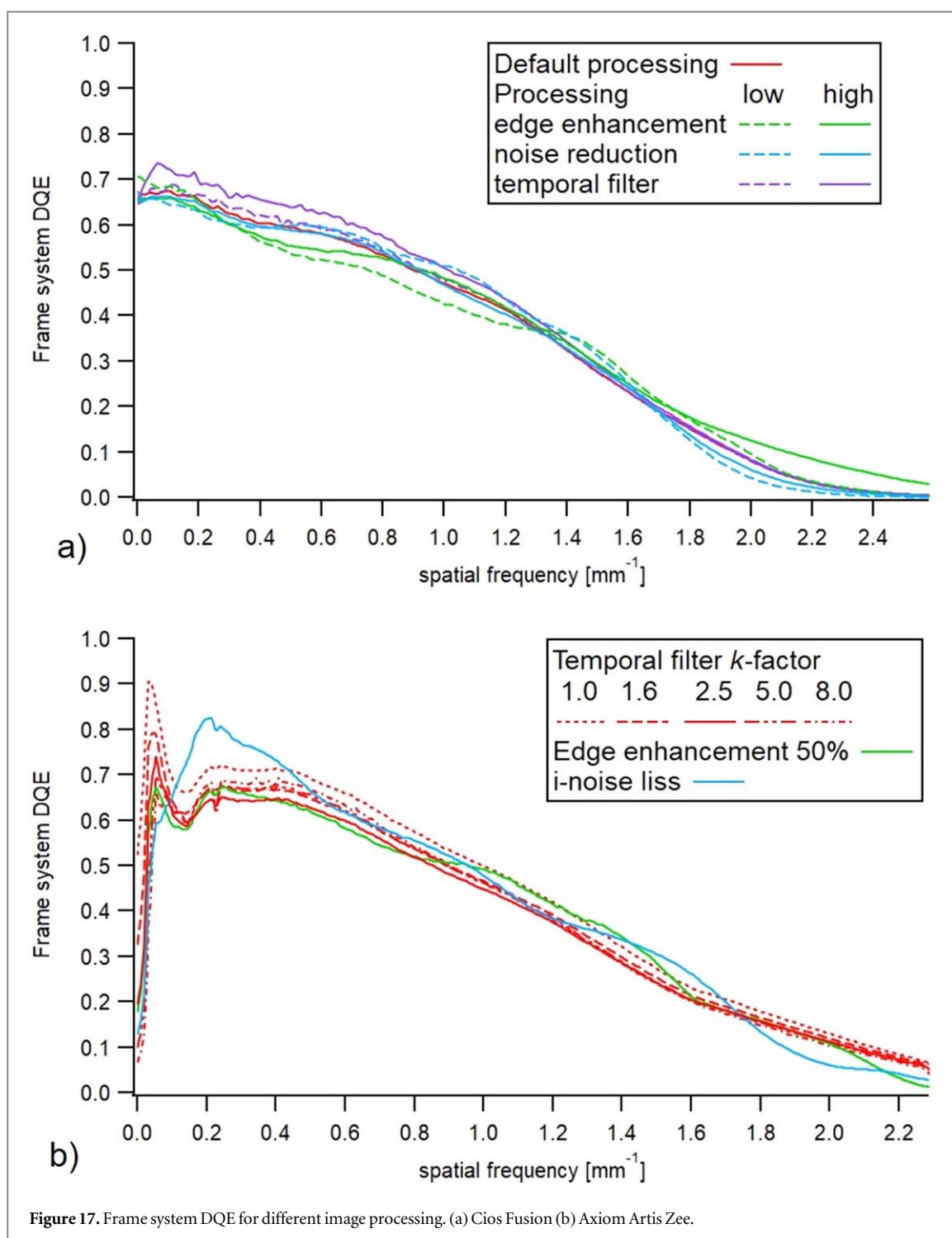
the SF, therefore $DQE_{\text{sys,frame}}$ increases with SF_{in} when the grid is in place and is independent of SF_{in} without grid. These results indicate that for the FOV $30 \times 30 \text{ cm}^2$, the grid increases the system efficiency only for SW thicknesses greater than 10 cm, and the grid should be removed for smaller thicknesses. This also explains why a decrease in the size of the x-ray beam collimation or an increase in the distance between the SW phantom and the grid entrance surface decreased $DQE_{\text{sys,frame}}$. For the Cios Fusion system, decreasing the FOV from $20 \times 20 \text{ cm}^2$ (beam B1) to $15 \times 15 \text{ cm}^2$ (beam B2) reduced $DQE_{\text{sys,frame}}$ from 0.65 to 0.50. An increase in the phantom-to-grid distance from 15 cm (beam B1) to 25 cm (beam B3) reduced $DQE_{\text{sys,frame}}$ from 0.65 to 0.55.

$DQE_{\text{sys,frame}}$ was independent of the dose rate for the Cios Fusion and Axiom Artis Zee systems (figure 16), as expected when the dose per frame is held constant by the AERC. For linear and shift invariant systems, $DQE_{\text{sys,frame}}$ is independent of image processing (Bernhardt *et al* 2005, Urbanczyk *et al* 2012). Edge enhancement, denoising and temporal processing roughly met these requirements in our study (figure 17). This



shows that these image processing procedures did not decorrelate the spatial MTF from the spatial NPS and the temporal MTF from the temporal NPS.

$DQE_{\text{sys,frame}}$ is a consistent metric to assess the overall efficiency of fluoroscopy systems in the presence of SF representative of clinical conditions encountered with patients. It includes the efficiency of the grid, the quantum efficiency of the detector, the spatial and temporal processing. The planar DQE used in radiography is irrelevant for fluoroscopy because the temporal bandwidth of the signal power is omitted, and a correction factor must be added to get the true values (Cunningham *et al* 2001, Friedman and Cunningham 2010). $DQE_{\text{sys,frame}}$ can further describe the effect of the spatial and temporal processing on the image quality, and can help in the framework of optimizing the imaging protocols in dynamic imaging. The standard detector DQE is determined for standardized primary beams obtained by using additional aluminium or copper filters, which do not meet at the same time the attenuation of the beam and the effective energy given by the AERC for a patient under clinical conditions. $DQE_{\text{sys,frame}}$ can be calculated for SW thicknesses that better mimic beam attenuation



and hardening, and SF produced by patients of different thicknesses. Compared to the standard detector DQE, the frame system DQE requires an additional measurement of SF_{in} . SF_{in} is essentially determined by the thickness of the SW phantom used for the measurement, the FOV and the air gap between the phantom and the grid. Standardized values of SF_{in} could be considered for routine use of $DQE_{sys,frame}$ in fluoroscopy.

4.8. Limitations of the method

Compared to planar NEQ and DQE, calculating the new metrics we are proposing requires an additional measurement of MTF_r . The temporal MTF is generally determined using moving sharp edges (Friedman and Cunningham 2006, 2009), and results from a ratio between two spatial MTFs measured with and without motion. The relative uncertainties of the two spatial MTFs add up, therefore the uncertainty in MTF is roughly doubled compared to in-plane MTF. The uncertainty in MTF_r adds to the uncertainty of spatial components in the estimation of NEQ_{frame} and $DQE_{sys,frame}$.

The processed images may contain nonlinear image processing which would make the MTF depend on contrast and noise (so, on dose). The assessment of image quality with transfer functions is a linear approximation of a nonlinear system and should thus be performed under restrictive conditions of small input signals, where the behaviour of the system can be considered as linear around an operating point (dose and contrast). The 0.1 mm thick copper disc used in this study for MTF measurement produced radiant contrasts between 13% and 33%, lower than the maximum contrast of 0.5 given by Friedman and Cunningham (2009) to meet the small signal requirement for the MTF calculation. The downside of small contrast is the low differentiation of the edge profile in the noise on the frames. An accurate MTF measurement in low CNR conditions requires a high number of frames to achieve sufficient overall CNR in the calculation. The number of frames chosen for the calculation of the MTF is a compromise between accuracy and computing time. In this study, the CNR given by the 0.1 mm copper disc on individual frames was approximately 0.2 for the reference conditions. Using 500 frames for each MTF measurement under static and dynamic conditions gave a total effective CNR of about 5.0. The effective CNR required to achieve a given accuracy and precision should be determined empirically from repeated MTF measurements under various CNR conditions (Chen *et al* 2014). This estimate was not made in our study. The exact extent to which nonlinear processing can degrade the MTF, NEQ and DQE has yet to be investigated, however the deviations in NEQ and DQE due to image processing shown in figure 17 provide insight into the uncertainty introduced by the different spatial and temporal image processing in the NEQ and DQE.

$DQE_{\text{sys,frame}}$ needs a measurement of SF_{in} that is not directly possible on fluoroscopy systems without special access to pre-processed images. The measurement of SF_{in} using the beam blocker method required additional images acquired on a radiography system on which the geometry and beam quality of the fluoroscopy systems are reproduced as close as possible. SW phantom thickness, beam collimation, distances, tube potential and additional copper filtration have been reported on the radiography system. Using different equipment can result in small variations in the amount of scatter produced by the tube itself and the radiological table. The influence of these radiations on SF_{in} remains low compared to the major contribution of scatter produced within the SW phantom thickness, but still constitutes an intrinsic limitation of the metrics.

5. Conclusion

This work introduced and tested new metrics to assess the image quality of dynamic imaging systems by considering the entire imaging system: the anti-scatter grid, the detector, and image processing techniques in the presence of scattered radiations. The frame NEQ and frame system DQE enable a comparison of imaging performance between fluoroscopy imaging protocols or fluoroscopy systems with different temporal resolutions. The new metrics we are proposing require the measurements of the temporal MTF and the input scatter fraction while providing a suitable method to evaluate and optimize dynamic imaging systems. These metrics provide access to benchmarking and quality control protocols for fluoroscopy systems without additional corrections for temporal resolution effects, as required when using planar NEQ and DQE.

References

- Akbarpour R, Friedman S N, Siewerdsen J H, Neary J D and Cunningham I A 2007 Signal and noise transfer in spatiotemporal quantum-based imaging systems *J. Opt. Soc. Am. A* **24** B151–64
- Anderson J A, Wang J and Clarke G D 2000 Choice of phantom material and test protocols to determine radiation exposure rates for fluoroscopy *Radiographics* **20** 1033–42
- Bernhardt P, Bätz L, Rührnschopf E-P and Hoheisel M 2005 Spatial frequency-dependent signal-to-noise ratio as a generalized measure of image quality *Proc. SPIE* **5745** 407–18
- Boone J M, Pfeiffer D E, Strauss K J, Rossi R P, Lin P-J P, Shepard J S and Conway B J 1993 A survey of fluoroscopic exposure rates: AAPM task group no. 11 report *Med. Phys.* **20** 789–94
- Boone J M and Seibert J A 1988 Monte Carlo simulation of the scattered radiation distribution in diagnostic radiology *Med. Phys.* **15** 713–20
- Boone J M and Seibert J A 1997 An accurate method for computer-generating tungsten anode x-ray spectra from 30 to 140 kV *Med. Phys.* **24** 1661–70
- Chen B, Christianson O, Wilson J M and Samei E 2014 Assessment of volumetric noise and resolution performance for linear and nonlinear CT reconstruction methods *Med. Phys.* **41** 071909
- Cunningham I A, Moschandreu T and Subotic V 2001 The detective quantum efficiency of fluoroscopic systems: the case for a spatial-temporal approach (or, does the ideal observer have infinite patience?) *Proc. SPIE* **4320** 479–88
- Dehairs M, Bosmans H, Desmet W and Marshall N W 2017 Evaluation of automatic dose rate control for flat panel imaging using a spatial frequency domain figure of merit *Phys. Med. Biol.* **62** 6610–30
- Dobbins J T 1995 Effects of undersampling on the proper interpretation of modulation transfer function, noise power spectra, and noise equivalent quanta of digital imaging systems *Med. Phys.* **22** 171–81
- Dobbins J T, Samei E, Ranger N T and Chen Y 2006a Intercomparison of methods for image quality characterization. I. Modulation transfer function *Med. Phys.* **33** 1454–65
- Dobbins J T, Samei E, Ranger N T and Chen Y 2006b Intercomparison of methods for image quality characterization. II. Noise power spectrum *Med. Phys.* **33** 1466–75

- Friedman S N and Cunningham I A 2006 A method to measure the temporal MTF to determine the DQE of fluoroscopy systems *Proc. SPIE* **6142** 61421X1–11
- Friedman S N and Cunningham I A 2009 A small-signal approach to temporal modulation transfer functions with exposure-rate dependence and its application to fluoroscopic detective quantum efficiency *Med. Phys.* **36** 3775–85
- Friedman S N and Cunningham I A 2010 A spatio-temporal detective quantum efficiency and its application to fluoroscopic systems *Med. Phys.* **37** 6061–9
- ICRU Report 54 1996 Medical imaging—the assessment of image quality *J. ICRU* **28** 31–9
- IEC 2005 Medical electrical equipment—radiation conditions for use in the determination of characteristics *IEC 61267* (Geneva: International Electrotechnical Commission)
- IEC 2008 Medical electrical equipment—characteristics of digital x-ray imaging devices: part 1–3. Determination of the detective quantum efficiency—detectors used in dynamic imaging *IEC 62220-1-3* (Geneva: International Electrotechnical Commission)
- Kyprianou I S, Rudin S, Bednarek D R and Hoffmann K R 2005 Generalizing the MTF and DQE to include x-ray scatter and focal spot unsharpness: application to a new microangiographic system *Med. Phys.* **32** 613–26
- Menser B, Bastiaens R J M, Nascetti A, Overdick M and Simon M 2005 Linear system models for lag in flat dynamic x-ray detectors *Proc. SPIE* **5745** 430–41
- Monnin P, Bosmans H, Verdun F R and Marshall N W 2016 A comprehensive model for quantum noise characterization in digital mammography *Phys. Med. Biol.* **61** 2083–108
- Monnin P, Verdun F R, Bosmans H and Marshall N W 2020 In-plane image quality and NPWE detectability index in digital breast tomosynthesis *Phys. Med. Biol.* **65** 095013
- Monnin P, Verdun F R, Bosmans H, Rodríguez Pérez S and Marshall N W 2017 A comprehensive model for x-ray projection imaging system efficiency and image quality characterization in the presence of scattered radiation *Phys. Med. Biol.* **62** 5691–722
- Rowlands J A 1984 Videofluororadiography: the role of temporal averaging *Med. Phys.* **11** 129–36
- Samei E, Flynn M J and Reimann D A 1998 A method for measuring the presampled MTF in digital radiographic systems using an edge test device *Med. Phys.* **25** 102–13
- Samei E, Ranger N T, MacKenzie A, Honey I D, Dobbins J T and Ravin C E 2009 Effective DQE (eDQE) and speed of digital radiographic systems: an experimental methodology *Med. Phys.* **36** 3806–17
- Siewerdsen J H, Cunningham I A and Jaffray D A 2002 A framework for noise-power spectrum analysis of multidimensional images *Med. Phys.* **29** 2655–71
- Smith S W and Kruger R A 1986 A signal processing model of diagnostic x-ray scatter *Med. Phys.* **13** 831–5
- Urbanczyk H, McDonagh E, Marshall N W and Castellano I 2012 Characterization of the effects of the Fine View algorithm for full field digital mammography *Phys. Med. Biol.* **57** 1987–2003
- Wilson D L, Jabri K N and Aufrichtig R 1999 Perception of temporally filtered x-ray fluoroscopy images *IEEE Trans. Med. Imaging* **18** 22–31
- Wilson D L, Jabri K N and Xue P 1997 Modeling human visual detection of low-contrast objects in fluoroscopy image sequences *Proc. SPIE* **3036** 21–30
- Zhao W and Rowlands J A 1997 Digital radiography using active matrix readout of amorphous selenium: theoretical analysis of detective quantum efficiency *Med. Phys.* **24** 1819–33